RSC Advances

PAPER

View Article Online
View Journal | View Issue

Cite this: *RSC Adv.*, 2025, **15**, 41381

Green-synthesized cardamom-modified iron oxide nanoparticles with potent antibacterial, antioxidant, anti-inflammatory, and anticancer activities

Swagota Briti Ray Gupta,[a] Shourav Paul,[b] Md. Abdul Momin,[c] Md. Faruk Hasan,[c] Md. Akhtar-E-Ekram,[a] Md. Salah Uddin,[a] Tariqul Hasan,[b] Md. Abu Saleh *[a] and Shahriar Zaman*[a]

Cancer and antimicrobial resistance pose significant global health challenges, necessitating the development of novel therapeutic approaches. This study presents the green synthesis of (3-aminopropyl)trimethoxysilane (APTMS)-modified iron oxide nanoparticles coated with *Elettaria cardamomum* extract (EC-AMIONPs) *via* a co-precipitation method. The synthesized nanoparticles were thoroughly characterized using UV-vis, FTIR, SEM, EDX, XRD, TGA, and VSM techniques. The analyses confirmed the successful formation of spherical, amorphous EC-AMIONPs with an average size of 14.28 nm and paramagnetic properties. Phytochemical screening revealed the presence of bioactive compounds, including terpenoids, steroids, alkaloids, tannins, and phenols. Functionally, EC-AMIONPs exhibited potent antioxidant activity (80.75% at 100 μg mL^{-1}), broad-spectrum antibacterial effects against multidrug-resistant pathogens, and significant antibiofilm capacity. The anti-inflammatory potential was demonstrated through the inhibition of albumin denaturation (76.92%), stabilization of HRBC membranes (78.85%), and proteinase inhibition (73.36%) at 200 μg mL^{-1}. Cytotoxicity, assessed *via* the *Artemia salina* assay, revealed moderate toxicity (65.00% lethality at 400 μg mL^{-1}; LC_{50}: 170.35 μg mL^{-1}), supporting their biosafety at therapeutic doses. *In vivo* studies in EAC-induced mice confirmed the anticancer efficacy of EC-AMIONPs, resulting in a significant reduction in tumor growth and improvement in physiological parameters, including hematological (RBC, WBC, hemoglobin), biochemical (ALT, creatinine, lipid profile), and ionic (Na^+, K^+, Ca^{2+}, Cl^-) profiles. Histological analysis further validated the protective effects on liver, kidney, lung, and intestinal tissues. Overall, EC-AMIONPs demonstrate multifunctional biomedical properties—antioxidant, antibacterial, anti-inflammatory, and anticancer—highlighting their potential as a green nanoplatform for future therapeutic applications.

Received 5th September 2025
Accepted 11th October 2025

DOI: 10.1039/d5ra06699a

rsc.li/rsc-advances

1. Introduction

Cancer has emerged as a leading cause of death globally, with a significant rise in cases over the past two decades attributed to lifestyle changes. This alarming trend underscores the urgent need for innovative approaches to cancer prevention and treatment.[1] Current cancer therapies primarily include chemotherapy, surgery, radiotherapy, immunotherapy, and hormonal therapy, with chemotherapy being the most prevalent despite its associated side effects and costs. The increasing issue of drug resistance has sparked interest in alternative treatments, such as metal ions (*e.g.*, iron, zinc), which have the potential to disrupt microbial enzymes, efflux pumps, and biofilms.[2,3] Traditional drug delivery methods, including oral, buccal, abdominal, subcutaneous, intramuscular, intravenous, pulmonary, and transdermal routes, often encounter challenges like slow absorption, side effects, instability, and uncontrolled release. In contrast, nanocarriers such as solid nanoparticles, liposomes, dendrimers, polymeric nanoparticles, micelles, virus-mimicking nanoparticles, carbon nanotubes, and mesoporous silica particles provide advanced solutions to these limitations.[4] Colloidal drug delivery systems (DDS) have proven particularly effective in diagnosing and treating brain and central nervous system (CNS) disorders.[5]

The green synthesis of nanoparticles presents a sustainable, eco-friendly, and cost-effective alternative to traditional methods by utilizing natural sources like plant extracts and microbes. This non-toxic approach holds significant promise

[a]*Microbiology Laboratory, Department of Genetic Engineering and Biotechnology, Faculty of Biological Sciences, University of Rajshahi, Rajshahi-6205, Bangladesh. E-mail: saleh@ru.ac.bd; szaman@ru.ac.bd*

[b]*Synthetic Functional Polymer Laboratory, Department of Chemistry, University of Rajshahi, Rajshahi-6205, Bangladesh*

[c]*Department of Microbiology, University of Rajshahi, Rajshahi-6205, Bangladesh*

for advancing cancer diagnosis and therapy, as well as tackling multidrug-resistant bacterial infections.[6] Green-synthesized nanoparticles play vital roles in diagnostics, therapy, and pharmaceuticals. They are also employed in environmental cleanup efforts, including water purification, heavy metal removal, and soil or wastewater treatment. Furthermore, they assist in controlling plant diseases and demonstrate strong antibacterial and antifungal properties by disrupting DNA or electron transport chains, ultimately leading to microbial death.[7] Moreover, functionalization of nanoparticles with biopolymers, phytochemicals, or ligands not only enhances their stability and biocompatibility but also improves targeting biological efficacy. Functionalized hydrogels can achieve stimuli-responsive drug release and enhanced tumor specificity.[8,9] Biowaste- or naturally derived nanoparticles offer a sustainable route for nanomaterial synthesis and applications in metal ion detection and information encoding.[10]

Nanoparticles (NPs) are structures ranging from 1 to 100 nm in size, encompassing viruses, lipoproteins, and intracellular assemblies such as magnetosomes. Surface modifications of NPs facilitate targeted delivery and specific biochemical interactions with cell receptors.[11,12] Nanotechnology finds applications across various fields, including animal health, agriculture, medicine, pharmaceuticals, nutrition, and the environment. NPs exhibit potent antibacterial, antifungal, and antiparasitic properties. In medicine, they play a crucial role in nanomedicine, nano-implants, and biosensors, enhancing diagnostics, targeted drug delivery, gene transfer, and treatments for conditions such as cancer, genetic disorders, neurological diseases, ocular issues, and heart diseases.[13–15] Magnetic iron oxide nanoparticles (MIONPs) are prone to aggregation and oxidation due to their high surface-to-volume ratio, which can diminish their magnetic properties and dispersibility. To improve stability and enable functionalization, protective coatings are applied, which can be either organic (such as surfactants and polymers) or inorganic (like silica and metals). While chemical synthesis of NPs may produce toxic byproducts, well-engineered iron oxide NPs have numerous medical applications, including cancer therapy, targeted drug delivery, immunoassays, tissue repair, detoxification, cell separation, hyperthermia, and enhanced MRI contrast.[16,17]

Herbal phytomedicines are garnering interest for their potential health benefits. Cardamom (*Elettaria cardamomum*), often referred to as the "Queen of Spices," is a perennial herb from the Zingiberaceae family, valued for its flavor, aroma, and medicinal qualities.[18] The therapeutic effects of cardamom stem from its abundance of bioactive compounds, particularly 1,8-cineole (over 50%), along with others such as limonene, terpineol, linalool, and α-pinene. These compounds contribute to cardamom's anti-inflammatory, anticancer, antibacterial, antifungal, cardioprotective, and gastroprotective properties. Additionally, flavonoids, terpenoids, anthocyanins, alkaloids, and phenolics found in cardamom are beneficial for treating diseases of the liver, kidney, lungs, and heart. Cardamom is widely utilized in both traditional and modern medicine for managing conditions such as asthma, digestive issues, vomiting, oral infections, and various renal and cardiovascular disorders.[19–21]

Recently, there has been increasing interest in synthesizing nanoparticles (NPs) using *E. cardamom* extract. Various NPs have been produced from *E. cardamom*, including TiO_2 NPs,[22] NiO NPs,[23] selenium NPs,[24] ZnO NPs,[25] CuO NPs,[26] gold and Ag NPs,[27] Co NPs,[28] and gelatin NPs.[5] In our study, we employed Soxhlet distillation to prepare a methanolic seed extract for synthesizing surface-modified iron oxide nanoparticles. These nanoparticles were modified using ATPMS through a co-precipitation method and assessed for their potential against oxidative stress, anti-inflammatory effects, multidrug-resistant bacteria, and cancer.

2. Materials and methods

2.1 Collection of plant materials

In January 2024, fresh, healthy green cardamom (*Elettaria cardamomum*) fruits were purchased from the RDA market in Rajshahi, Bangladesh, for use in the current studies.

2.2 Preparation of EC-AMIONPs

2.2.1 Preparation of *E. cardamomum* extract. The Soxhlet distillation technique, with necessary modifications, was employed to prepare the cardamom extract.[29] After washing the fruits and air drying them, they were ground into a coarse powder using an electric grinder. Approximately 300 g of the dried, ground plant material was subjected to successive extraction with methanol using a Soxhlet apparatus. The solvents were then evaporated under reduced pressure, resulting in a cream powder of the extract, which was stored at 4 °C.

2.2.2 Synthesis of magnetic iron oxide nanoparticles (MIONPs). MINOPs were synthesized using the co-precipitation method, a widely recognized technique.[30] To prepare the nanoparticles, $FeCl_3 \cdot 6H_2O$ and $FeSO_4 \cdot 7H_2O$ were dissolved in deionized water at a 2 : 1 molar ratio and heated to 80 °C with constant stirring. A 25% NH_4OH solution was added dropwise to raise the pH to 10–11, causing the solution to turn black, indicating nanoparticle formation. After stirring for 60 minutes, the particles were allowed to settle, washed with ethanol and water, magnetically separated, and then dried in a vacuum oven at 80 °C for 24 hours.

2.2.3 Surface modification of prepared iron oxide nanoparticles by APTMS. APTMS was used to modify the outer coating of Fe_2O_3 nanoparticles (AMIONPs), with minor adjustments made based on earlier research.[31] A total of 5.0 g of iron oxide nanoparticles was ultrasonically dispersed in 50 mL of anhydrous toluene for 30 minutes. Following this, acid hydrolysis was conducted at pH 1.5–2 for 1 hour. The pH was then adjusted to 8–9 using 50% NaOH, and condensation proceeded for 2 hours. Next, 1 mL of APTMS was added dropwise while maintaining continuous ultrasonication. The mixture was sonicated at 80 °C for 6 hours under nitrogen to prevent oxidation. The modified nanoparticles were then magnetically separated, washed with ethanol and toluene, and vacuum-dried overnight at 60 °C.

2.2.4 Synthesis of AMIONPs using *E. cardamomum* extract. Fifty mg of APTMS-coated iron oxide nanoparticles were dispersed in THF and activated with NHS. Separately, cardamom extract and EDC were mixed in THF for carbodiimide activation. The extract-EDC solution was then added to the nanoparticle mixture and sonicated for 2 hours at room temperature to facilitate conjugation. The resulting nanoparticles were magnetically separated, washed with ethanol, and stored in PBS at 4 °C.

2.3 Characterization of synthesized EC-AMIONPs

UV-vis spectroscopy was employed to assess the stability of EC-AMIONPs suspensions. Absorbance was measured between 200–400 nm using a Thermo Scientific Evolution 201 spectrophotometer in SDA mode, with a 30 ms integration time and a scan speed of 2000 nm min^{-1}.[32] The functional groups and chemical structure of the produced AMIONPs and EC-AMIONPs were analyzed using Fourier transform infrared (FTIR) spectroscopy, employing a KBr pellet to describe the solution in the 4000–500 cm^{-1} range. The universe disc was examined for this experiment.[33] The size and shape morphology of synthesized AMIONPs and EC-AMIONPs were characterized using scanning electron microscopy (SEM) (Germany) with a maximum magnification of 300 000× and a resolving power of 2.3 nanometers, which revealed surface topology and composition.[34] The crystallinity and phase purity of AMIONPs and EC-AMIONPs were analyzed using X-ray diffraction (XRD) (PANalytical Pro Diffractometer) with Cu Kα radiation (λ = 0.15406 nm, 40 kV, 30 mA). The average particle size was calculated using the Debye–Scherrer equation from the diffraction data collected over a range of 2θ angles.[35] The magnetic properties of AMIONPs and EC-AMIONPs in powder form were investigated in air at 300 K with a field strength of up to 15 000 G using a vibrating sample magnetometer (VSM, Lake Shore 7410). Energy-dispersive X-ray spectroscopy (EDX) confirmed the presence of iron and oxygen in AMIONPs and EC-AMIONPs, indicating successful synthesis and surface modification. This analysis was performed using an Oxford Inca Penta FeTX3 EDS attached to a Carl Zeiss Evo MA 15 SEM.[36] Finally, thermogravimetric analysis (TGA) was conducted to evaluate the thermal stability of AMIONPs and EC-AMIONPs, heating from 30 °C to 800 °C at a rate of 20 °C min^{-1} under nitrogen flow (60 mL min^{-1}).

2.4 Qualitative phytochemical analysis

Standard procedures were employed to screen for various phytochemicals in EC-AMIONPs. The EC extract and EC-AMIONPs were tested for the presence of flavonoids (HCl test),[37] steroids (Salkowski's test),[38] tannins and phenols (ferric chloride test),[37] alkaloids (Mayer's reagent test),[37] carbohydrates and glycosides (Fehling's solution test),[39,40] and terpenoids (sulfuric acid test).[41] Each plant sample was analyzed three times. Qualitative results were denoted as (+) for the presence and (−) for the absence of phytochemicals.

2.5 Determination of antibacterial activity by the disc diffusion method

The antibacterial efficacy of EC-AMIONPs was evaluated against 12 highly emergent multidrug-resistant bacteria, both Gram-negative and Gram-positive. A modified disc diffusion method[42] was utilized to assess the antibacterial activity of EC-AMIONPs against the following pathogenic bacteria: *E. coli* (ATCC 35401), *Pseudomonas aeruginosa* (ATCC BAA-2108), *Acinetobacter lactucae* (ATCC TSD-58), *Aeromonas* spp. (ATCC 49140), *Enterobacter cloacae* (ATCC BAA-2468), *Staphylococcus aureus* (ATCC 13565), *Bacillus* sp. (ATCC 14579), *Shigella sonnei* (ATCC 25931), *Enterobacter* spp. (ATCC 21754), *Staphylococcus epidermidis* (ATCC 35984), *Shigella flexneri* (ATCC 12022), and *Salmonella typhi* (ATCC 6539). The A extract and EC-AMIONPs (1 mg mL^{-1} each) were sonicated for 30 minutes, and 50 μg per disc was applied to 5 mm Whatman filter discs. Subsequently, a bacterial suspension (1×10^6 CFU mL^{-1}) was transferred from an overnight culture and gently spread on Mueller–Hinton Agar (MHA) plates, then incubated at 37 °C for 24 hours. The zones of inhibition were measured in millimeters and compared to clarithromycin (15 μg per disc).

2.6 Determination of anti-biofilm assay of EC-AMIONPs

2.6.1 Biofilm formation activity. The biofilm formation test was conducted using a modified microtiter plate (MtP) assay protocol.[43] Selected pathogenic bacteria were cultured in LB broth at 37 °C for 24 hours and then adjusted to an optical density (OD) of 1.0 at 640 nm. A total of 100 μL of the bacterial suspension was added to each well of a 96-well microtiter plate and incubated statically at 37 °C for 24 hours to encourage biofilm formation. After incubation, the wells were washed twice with double-distilled water and stained with 0.1% crystal violet for 60 minutes. The stained biofilms were then rinsed twice with phosphate buffer and air-dried for approximately one hour. To quantify biofilm formation, the bound crystal violet was solubilized, and absorbance was measured at 595 nm using a microplate reader. The OD_{595} values reflected the biofilm quantity for each strain, with the strongest biofilm-forming strain selected for further anti-biofilm testing.

2.6.2 Inhibition of biofilm formation by EC-AMIONPs. The anti-biofilm activity of EC-AMIONPs was assessed using a previously established method.[41] To each well of the 96-well microtiter plate, 100 μL of bacterial suspension was added, followed by 100 μL of either EC or EC-AMIONPs, resulting in a total volume of 200 μL per well. For control purposes, bacterial suspensions and liquid media were used instead of EC and EC-AMIONPs, with three replicates for each condition. After following the procedure, the optical density was measured at 620 nm using a multiplate reader. The biofilm inhibition efficiency was calculated using the equation below.[44]

$$\text{Biofilm inhibition (\%)} = \frac{1 - \text{OD of EC-AMIONPs treated cells}}{\text{OD of control}} \times 100$$

2.7 Determination of antioxidant activity by DPPH scavenging assay

To evaluate the DPPH (2,2-diphenyl-1-picrylhydrazyl) free radical scavenging potential of EC-AMIONPs, a spectrophotometric method was employed[45] with minor modifications. A 0.4 mM solution of DPPH and BHT (butylated hydroxytoluene) was prepared in 100% methanol. The reaction mixtures included 2 mL of 0.4 mM DPPH combined with 2 mL of either EC, EC-AMIONPs, or BHT (as a standard) at concentrations of 40, 60, 80, and 100 μg mL^{-1}. These mixtures were incubated in the dark at 25 ± 2 °C for 30 minutes. After incubation, absorbance was measured at 570 nm using a spectrophotometer, with methanol-DPPH serving as the control and BHT as the standard. The percentage of free radical scavenging activity (% RSA) of EC-AMIONPs was calculated using the following formula:

$$\%\ \mathrm{RSA} = \frac{(\mathrm{control} - \mathrm{sample})}{\mathrm{control}} \times 100$$

2.8 Determination of anti-inflammatory assay of EC-AMIONPs

2.8.1 Albumin denaturation assay. The *in vitro* anti-inflammatory potential of EC-AMIONPs was assessed using a modified BSA denaturation method.[46] EC, EC-AMIONPs, and diclofenac sodium (as a standard) were dissolved in methanol to create stock solutions at 1 mg mL^{-1}. From these, five concentrations (50, 75, 100, 150, and 200 μg mL^{-1}) were prepared using PBS (pH 6.8). Each sample was combined with 1000 μL of 1% BSA and 1400 μL of PBS in test tubes, then incubated at 37 °C for 15 minutes before being heated at 72 °C for 5 minutes. After cooling, absorbance was measured at 660 nm against a blank. The percentage of inhibition was calculated, and IC_{50} values were derived from the regression line of inhibition *versus* concentration. The inhibition percentage (indicating protein denaturation) was determined from three repeated experiments using the following equation:

$$\%\ \text{inhibition BSA} = \frac{1 - A_{\mathrm{sample}}}{A_{\mathrm{control}}} \times 100$$

2.8.2 HRBC membrane stabilization assay

2.8.2.1 Preparation of HRBC suspension. Blood samples were obtained from healthy volunteers who had not taken NSAIDs for at least two weeks. The blood was mixed 1 : 1 with sterile Alsever's solution (composed of 2.05% dextrose, 0.8% sodium citrate, 0.055% citric acid, and 0.42% sodium chloride in 100 mL distilled water), adjusted to a pH of 6.0–7.0, and centrifuged at 3000 rpm for 15 minutes. The HRBC pellet was washed three times with isotonic saline and stored at 4 °C for 24 hours. A 10% HRBC suspension was then prepared in isotonic saline for the membrane stabilization assay.[47]

2.8.2.2 HRBC membrane stabilization method. The membrane stabilization activity of EC-AMIONPs was evaluated using a modified HRBC membrane stabilization method.[48] Different concentrations (50, 75, 100, 150, and 200 μg mL^{-1}) of EC extract, EC-AMIONPs, and diclofenac sodium were prepared, along with a blank that did not contain extract or standard. Each test mixture included 1 mL of phosphate buffer, 2 mL of hyposaline, and 0.5 mL of HRBC suspension. Samples were incubated at 37 °C for 30 minutes and then centrifuged at 3000 rpm for 10 minutes. Hemoglobin release in the supernatant was measured at 560 nm to evaluate membrane stabilization. The IC_{50} value was determined by plotting the percentage of inhibition against concentration and calculating a regression line. Both the proportion of protection and the percentage of hemolysis were calculated.

$$\%\ \text{protection} = \frac{(\mathrm{OD}_{\mathrm{control}} - \mathrm{OD}_{\mathrm{sample}})}{\mathrm{OD}_{\mathrm{control}}} \times 100$$

2.8.3 Proteinase inhibitory assay. The proteinase inhibitory activity of EC-AMIONPs was assessed using a modified trypsin method.[49] Methanol solutions of EC extract, EC-AMIONPs, and diclofenac sodium (the standard) were prepared at concentrations of 50, 75, 100, 150, and 200 μg mL^{-1}. For each 1 mL sample, 0.06 mg of trypsin and 1 mL of 20 mM Tris–HCl buffer were added and incubated at 37 °C for 15 minutes. After this, 1 mL of 0.8% casein was introduced, and the mixture was incubated for an additional 20 minutes. The reaction was halted by adding 2 mL of 70% perchloric acid, followed by centrifugation at 3000 rpm for 5 minutes. The absorbance of the supernatant was measured at 210 nm, with a blank containing no sample or standard serving as the control. The IC_{50} value was determined by plotting the percentage inhibition against the sample concentration and deriving a regression line. The percentage of inhibition (protein denaturation) from three repeated experiments was calculated using the following equation:

$$\%\ \text{inhibition of denaturation} = \frac{1 - A_{\mathrm{sample}}}{A_{\mathrm{control}}} \times 100$$

2.9 Brine shrimp nauplii toxicity assay

To evaluate acute toxicity, a brine shrimp lethality assay was conducted using EC-AMIONPs at concentrations of 50, 100, 200, and 400 μg mL^{-1}. Artificial seawater was prepared by dissolving 38 g of NaCl in 1000 mL of distilled water. Brine shrimp cysts (1 g) were hatched in this solution under continuous light and aeration at 30 °C for 24 hours. Following hatching, 20 nauplii were transferred to each well of a 12-well plate containing 2 mL of saline and test samples. Control wells contained no nanoparticles, and all treatments were performed in triplicate. The plates were then incubated in the dark for 24 hours, after which the number of surviving nauplii was counted. Toxicity was assessed by calculating death rates and determining the LC_{50} value using GraphPad Prism software, with results compared to the control group.[50,51] The formula used to calculate percentage mortality is as follows:

$$\text{Mortality}\ (\%) = \frac{\text{number of dead } A.\ salina \text{ nauplii}}{\text{initial number of live } A.\ salina \text{ nauplii}} \times 100$$

2.10 *In vivo* anti-cancer activity of EC-AMIONPs

2.10.1 Experimental animals. Male Swiss albino mice (22–24 g) were selected to minimize hormonal variability and ensure consistent results in cancer progression and treatment studies. The mice were housed in polypropylene cages under controlled conditions (24 ± 2 °C, 12-hour light/dark cycle, 60 ± 5% humidity) and were fed a standard diet for five days to allow for acclimatization. The experiment was conducted once to maintain methodological consistency.

2.10.2 Experimental groups. Following the acclimatization period, the mice were randomly assigned to five experimental groups, each consisting of six animals ($n = 6$). The groups were organized as follows: the first group served as the normal control and received only a standard diet (normal group). The second group included mice injected with EAC cells without treatment (affected group). The third group comprised EAC-induced mice treated with EC-AMIONPs (EC-AMIONPs-treated group). The fourth group received EC-extract following EAC cell induction (EC-extract-treated group). The fifth group was treated with the standard chemotherapeutic drug doxorubicin after EAC cell induction (doxorubicin-treated group). The final group consisted of EAC-induced mice treated with a combination of doxorubicin and EC-AMIONPs (EC-AMIONPs-DOX treated group).

2.10.3 Collection and maintenance of EAC cell line. Ehrlich ascites carcinoma (EAC) was obtained from the Department of Biochemistry and Molecular Biology at the University of Rajshahi. The EAC cell culture and aspiration were maintained following the method described by Alam.[52] EAC cells were harvested from a donor Swiss albino mouse with 6–7-day-old ascites tumors. On the sixth day, the mouse was sacrificed, and the cells were harvested using 1% NaCl, then incubated at 37.5 °C for one hour. Macrophages adhered to the dish surface, facilitating the separation from the free-floating EAC tumor cells.[53] The dish was briefly vortexed to release the EAC cells, which were then collected and diluted in 0.9% normal saline to a concentration of 3×10^6 cells per mL. Cell counts were performed using a hemocytometer, and viability was assessed *via* 0.4% trypan blue exclusion. All steps were conducted under aseptic conditions to maintain sterility for transplantation.

2.10.4 Treatment administration and cell growth inhibition. The assessment of *in vivo* cancer cell growth inhibition was conducted using a standard and straightforward procedure based on a previously established method.[54] Swiss albino mice were divided into six groups to evaluate the anti-cancer activity of EC-AMIONPs. All mice, except for the normal control group, received an intraperitoneal injection of 20 μL EAC cells (3×10^6 cells per mL) on day 0. Treatments commenced 36 hours after injection and continued for five days. Group I received only a standard diet (normal group), group II received EAC cells without treatment (affected group), group III was treated with EC-AMIONPs (0.2 mg kg^{-1} day^{-1}), group IV with EC extract (0.2 mg kg^{-1} day^{-1}), group V with a single dose of doxorubicin (0.1 mg kg^{-1}), and group VI with a combination of EC-AMIONPs and doxorubicin (0.2 mg kg^{-1} day^{-1}). On day 15, all mice were sacrificed, and peritoneal fluid was collected for EAC cell analysis.

Viable tumor cells were counted using a hemocytometer and trypan blue exclusion. The results were compared with those of the untreated EAC group to assess tumor inhibition using the following formula:

$$\text{Cells per mL} = \frac{\text{the average count per square} \times \text{dilution factor}}{\text{depths of fluid under cover slip} \times \text{area counted}}$$

The percentage of cell growth inhibition was calculated by comparing the total number of viable cells in the treated groups to those in the control group, using the following equation:

$$\%\ \text{of growth inhibition} = \left(1 - \frac{\text{cells from different groups of treated mice}}{\text{cells from control mice containing EAC cells}}\right) \times 100$$

2.10.5 Evolution of body weight and glucose level. Body weight and blood glucose levels were monitored on days 0, 3, 5, 7, 9, 11, 13, and 15 following EAC inoculation. Mouse weights were recorded using an electronic balance, and glucose levels were measured from tail vein blood samples with a glucose monitoring sensor.

2.10.6 Biochemical, hematological, and ionic parameters. At the conclusion of the experiment on day 15, blood samples were collected from each mouse for biochemical and electrolyte analysis. Plasma levels of creatinine, total cholesterol, triglycerides, and ALT were measured, along with the concentrations of Na^+, K^+, Ca^{2+}, and Cl^-, using an automated clinical chemistry analyzer (CHEMIX-800, Japan). For hematological analysis, blood was drawn *via* cardiac puncture, and the total RBC count, hemoglobin, and WBC count were determined using the same analyzer.[55,56]

2.10.7 Histological analysis. For histopathological evaluation, excised tissue samples (liver, lung, heart, kidney, spleen, and intestine) were fixed in 10% formaldehyde for 24 hours. The tissues were then dehydrated in graded alcohol, embedded in paraffin, and sectioned to a thickness of 5 μm. Sections were stained with hematoxylin and eosin (H&E) and periodic acid–Schiff (PAS) stains. Microscopic examination was performed to assess tissue architecture and identify any pathological alterations or inflammation related to EAC cell proliferation or treatment effects. Tissues from both control and treated groups were analyzed and compared.[57]

2.11 Statistical analysis

GraphPad Prism was used to analyze data, and all values were reported as the mean ± standard error (SE). A significant test was used to analyze all the data.

3. Results

3.1 Synthesis of iron oxide nanoparticles using *E. cardamomum*

After modifying the surface with (3-aminopropyl)trimethoxysilane (APTMS), the nanoparticles changed color from

deep black to a slightly brownish-black, indicating successful silane attachment. This color shift is due to the interaction between the silane groups and the iron oxide nanoparticles. Using EDC–NHS coupling, carboxyl (–COOH) groups were activated for biomolecule binding. When biomolecules from *E. cardamomum* extract were added, the solution darkened to a deep brown-black, confirming covalent attachment, with the intensity of the color varying according to the concentration of the biomolecules.

3.2 Characterization of EC-AMIONPs

3.2.1 UV-vis spectroscopy. The UV-visible absorption spectra of the EC extract showed a peak at approximately 204 nm, whereas the EC-AMIONPs displayed peaks at 219 nm and 275 nm (Fig. 1A). These UV-visible bands indicate that Fe ions were modified by the EC seed extract, with the highest absorption peak at 219 nm confirming the formation of EC-AMIONPs.

3.2.2 Fourier transform infrared spectroscopy (FTIR) analysis. FTIR analysis confirmed the modification of iron oxide nanoparticles with ATPMS and their bioconjugation with *E. cardamomum* extract using the EDC–NHS method. The formation of amide bonds and shifts in functional group peaks provided strong evidence of covalent binding, as shown in Fig. 1B and Table 1.

A prominent absorption peak in the 570–580 cm^{-1} range indicated the Fe–O stretching vibration, confirming the presence of iron oxide nanoparticles. The intensity of the Fe–O peak at 578 cm^{-1} slightly decreased due to the organic coating, further supporting the surface modification. The Si–O peak around 1138 cm^{-1} confirmed the core–shell structure and indicated successful salinization. Additionally, the presence of

Table 1 Different functional groups in EC-AMIONPs

Functional group	Wavenumber (cm^{-1})
$–NH_2$	3408
–CH	2924
Si–O	1138
Fe–O	578
CONH	1650

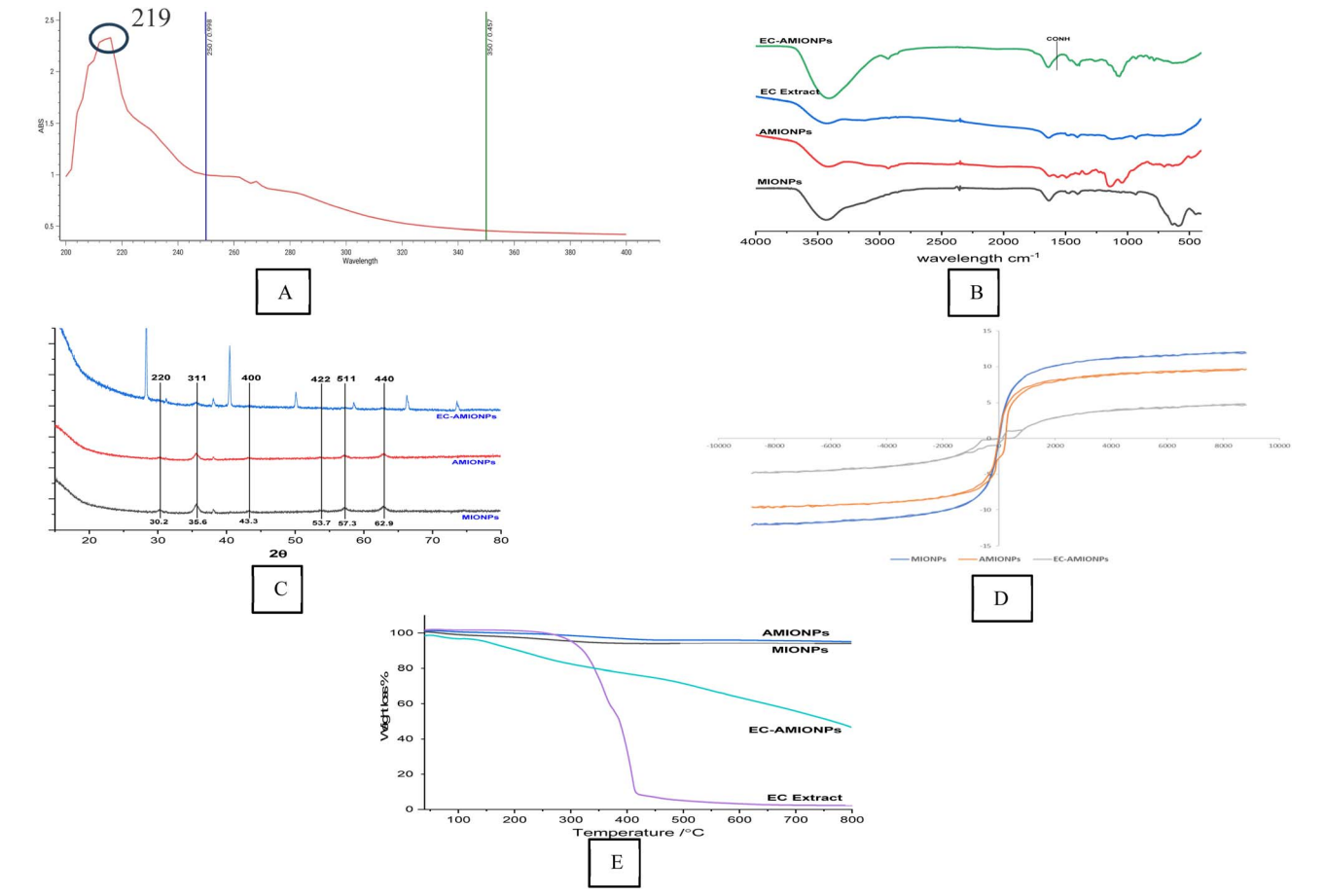

Fig. 1 Characterization of EC-AMIONPs using UV-vis spectroscopy (A) and the functional groups present in the biosynthesized EC-AMIONPs detection by FTIR analysis (B), confirmed the particle synthesis. Analysis of EC-AMIONPs size using X-ray diffraction spectrometry (C), magnetic behavior using vibrating sample magnetometry (VSM) (D), and thermogravimetric analysis (TGA) (E) was employed to evaluate the thermal properties and stability of EC-AMIONPs.

a peak at approximately 2924 cm^{-1} (C–H stretching) confirmed the incorporation of propyl (–CH_2 groups from ATPMS). Shifts in the hydroxyl and amine peaks (N–H) at 3408 cm^{-1} suggested hydrogen bonding and molecular interactions. The CONH peak at 1650 cm^{-1} indicated successful activation of carboxyl groups by EDC–NHS and subsequent formation of amide linkages with amine groups from biomolecules in *E. cardamomum*.

3.2.3 X-ray diffraction spectrometry (XRD) analysis. X-ray diffraction (XRD) analysis confirmed that AMIONPs possess a highly crystalline cubic spinel structure, exhibiting distinct peaks at 2θ values of 30.2°, 35.6°, 43.3°, 57.3°, and 62.9°, which correspond to specific crystal planes (Fig. 1C). In contrast, the peaks for EC-AMIONPs showed decreased intensity and slight broadening, suggesting that polyphenolic compounds modified the surface and reduced crystallinity. Importantly, no new peaks emerged, indicating that the compounds from *E. cardamomum* formed an amorphous coating without altering the underlying crystal structure. The average size of the nanoparticles, determined using the Debye–Scherrer equation, was found to be 14.48 nm (Table 2).

3.2.4 Vibrating sample magnetometer (VSM). The VSM curve of unmodified iron oxide nanoparticles displayed superparamagnetic behavior. The observed reduction in magnetization indicated successful functionalization, resulting in decreased magnetic dipole interactions (Fig. 1D). These results suggest that the synthesized nanoparticles maintain paramagnetic properties, making them suitable for biomedical and environmental applications.

3.2.5 Thermogravimetric analysis (TGA). Thermogravimetric analysis (TGA) of EC-AMIONPs (Fig. 1E) revealed an initial weight loss of 20% below 400 °C, attributed to moisture evaporation. Between 400 °C and 800 °C, a gradual weight loss of 50% occurred, corresponding to the decomposition of organic compounds from the cardamom extract, thereby confirming surface modification. Above 800 °C, the presence of a stable residue indicated the existence of thermally stable nanoparticles, further confirming successful functionalization with cardamom biomolecules.

3.2.6 Scanning electron microscopy (SEM). SEM analysis revealed that unmodified iron oxide nanoparticles were quasi-spherical with slight agglomeration (Fig. 2a). Following ATPMS coating, the particles maintained their spherical shape but appeared slightly larger, featuring a visible thin organic layer (Fig. 2b). Further modification with *E. cardamomum* extract resulted in a rougher surface and increased size due to biomolecular adsorption, enhancing dispersion and reducing aggregation while preserving the spherical shape (Fig. 2c). The EC-AMIONPs were spherical and well-dispersed (Fig. 2d).

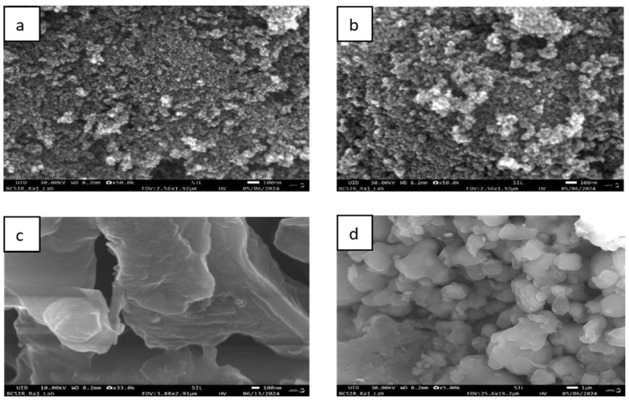

Fig. 2 SEM analysis of particle size and morphology (a) MIONPs, (b) AMIONPs, (c) EC extract, (d) EC-AMIONPs; the size was calculated by ImageJ software.

3.2.7 The energy dispersive X-ray spectroscopy (EDX). The results indicated a prominent peak for Fe ions, confirming the presence of iron in its metallic form, as shown in Fig. 3. The spectrum displayed strong peaks for iron (Fe) at 43.40% and oxygen (O) at 37.57%, signifying the formation of iron oxide nanoparticles (Fig. 3b). Additionally, minor peaks were observed for carbon (C) at 16.45% and other elements, such as silicon (Si) at 0.98%, primarily associated with modification using ATPMS (Fig. 3b). However, the EC extract showed no detectable iron (Fe) or silicon (Si) components (Fig. 3c). The presence of these elements indicates successful surface modification and functionalization of the nanoparticles. Furthermore, the absence of significant impurity peaks reinforces the purity of the synthesized material (Table 3).

3.3 Qualitative phytochemical analysis

The phytochemical analysis of cardamom's methanol extract revealed the presence of terpenoids, steroids, alkaloids, flavonoids, carbohydrates, glycosides, tannins, and phenols. In contrast, the EC-AMIONPs analysis indicated a positive presence of terpenoids, steroids, alkaloids, tannins, and phenols, as detailed in Table 4.

3.4 Biomedical application of EC-AMIONPs

3.4.1 Antibacterial activity. The antibacterial activity of EC-AMIONPs demonstrated significant inhibition zones against

Table 2 The Miller indices, Bragg's diffraction angle, FWHM, and the size of EC-AMIONPs

		FWHM β		Particle size (nm)		Average particle size (nm)	
Miller indices	2θ	MIONPs	AMIONPs	MIONPs	AMIONPs	MIONPs	AMIONPs
220	30.2	0.61	0.59	13.48392	13.941	13.22	14.48
311	35.6	0.72	0.69	11.58397	12.08762		
400	43.3	0.59	0.57	14.48123	14.98935		
511	57.3	0.64	0.57	14.13926	15.87566		
440	62.9	0.75	0.60	12.41157	15.51447		

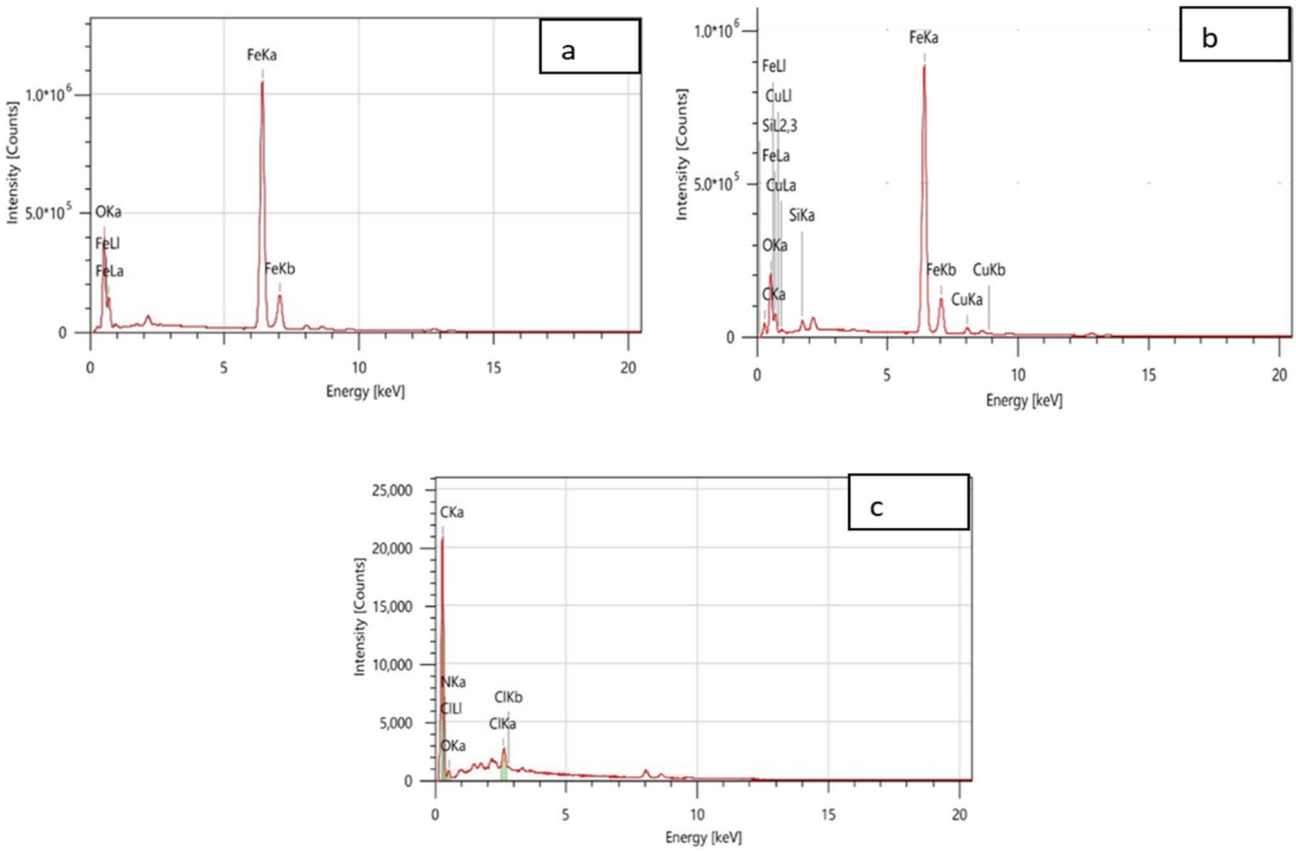

Fig. 3 The nanomaterials' elemental detail and their composition using EDX. MIONPs (a), EC-AMIONPs (b), EC extract (c).

Table 3 The elemental composition of the biosynthesized EC-AMIONPs

Sample	C atom%	O atom%	Fe atom%	Si atom%
MIONPs	—	42.32	57.68	—
EC-AMIONPs	16.45	37.57	43.40	0.98
EC extract	78.18	20.98	—	—

various bacteria: *E. coli* (28 ± 2 mm), *P. aeruginosa* (24 ± 2 mm), *A. lactucae* (33 ± 2 mm), *A.* spp. (30 ± 2 mm), *E. cloacae* (28 ± 2 mm), *Bacillus* sp. (30 ± 2 mm), *S. sonnei* (19 ± 2 mm), *E.* spp. (25 ± 2 mm), *S. flexneri* (19 ± 2 mm), and *S. typhi* (27 ± 2 mm). There was weak activity observed against *S. epidermidis*, with no activity against *S. aureus*. In contrast, the EC extract showed strong inhibition zones against *E. coli* (24 ± 2 mm), *A. lactucae* (27 ± 2 mm), *A.* spp. (21 ± 2 mm), *E. cloacae* (24 ± 2 mm), and *Bacillus* sp. (21 ± 2 mm). The results are illustrated in Fig. 4A.

3.4.2 Anti-biofilm activity of EC-AMIONPs

3.4.2.1 Biofilm inhibition of the EC-AMIONPs. The results demonstrated a significant reduction in biofilm formation when the strains were treated with EC-AMIONPs. Notable anti-biofilm activity was observed against *E. coli* (87.97%), *P. aeruginosa* (81.62%), *A. lactucae* (89.04%), *A.* spp. (87.44%), *E.* spp. (85.78%), *S. typhi* (83.79%), and *S. aureus* (83.39%). The lowest anti-biofilm activity was recorded against *S. flexneri* (60.78%). The effectiveness of EC-AMIONPs in inhibiting biofilm formation in bacterial pathogens is illustrated in Fig. 4B.

3.4.3 Anti-inflammatory activities

3.4.3.1 Albumin denaturation assay. The albumin denaturation assay for biosynthesized EC-AMIONPs is presented in Fig. 4C. The highest inhibition of protein denaturation for albumin was recorded at 76.92% with a concentration of 200 μg mL^{-1} of EC-AMIONPs, compared to 79.51% for diclofenac sodium and 57.45% for the plant extract. These results indicate that EC-AMIONPs more effectively inhibited albumin

Table 4 Phytochemical analysis of EC-AMIONPs[a]

Sample	Flavonoid	Steroid	Terpenoid	Tannin	Phenol	Alkaloid	Carbohydrate	Glycoside
EC extract	+	+	+	+	+	+	+	+
EC-AMIONPs	−	+	+	+	+	+	−	−
Residue	+	−	−	−	−	−	+	+

[a] "+" = presence; "−" = absent.

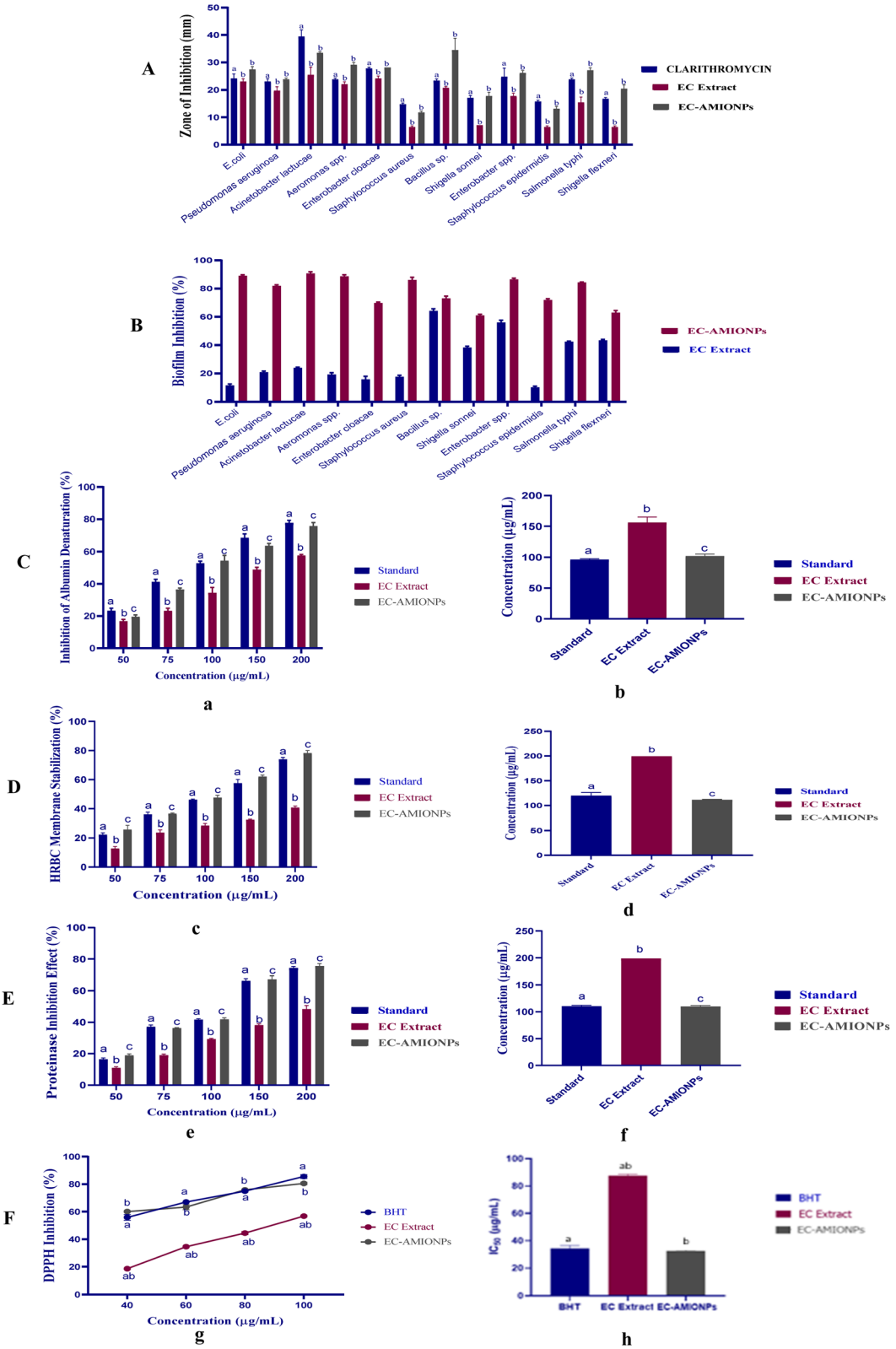

Fig. 4 Biomedical application of EC-AMIONPs antibacterial activity against 12 pathogenic bacteria (A) and (B) biofilm inhibition percentage. (C) Albumin denaturation assay; albumin denaturation percentage (a), IC_{50} value (b). (D) HRBC membrane stabilization assay; HRBC membrane stabilization percentage (c), IC_{50} value (d). (E) Proteinase inhibitory assay; proteinase inhibition percentage (e) and the IC_{50} value (f). (F) Anti-oxidant activity; DPPH inhibition percentage (g) and the IC_{50} value (h) of EC-AMIONPs.

denaturation than both the EC extract and the control, as illustrated in Fig. 4C(a). The IC_{50} values for the EC extract, diclofenac sodium, and EC-AMIONPs were 101.52 ± 4.842 μg mL^{-1}, 97.96 ± 4.842 μg mL^{-1}, and 155.56 ± 4.842 μg mL^{-1}, respectively, indicating the concentration at which 50% mortality was achieved, as shown in Fig. 4C(b).

3.4.3.2 HRBC membrane stabilization assay. Fig. 4D displays the HRBC membrane stabilization assay for biosynthesized EC-AMIONPs. EC-AMIONPs, EC extracts, and diclofenac sodium at varying concentrations (50, 75, 100, 150, and 200 mg mL^{-1}) demonstrated significant stabilization of HRBC membranes. At a concentration of 200 mg mL^{-1}, EC-AMIONPs provided 78.85% protection, which was greater than at the other concentrations, although overall protection increased with higher concentrations. The results are shown in Fig. 4D(c). The IC_{50} values for the EC extract, diclofenac sodium, and EC-AMIONPs were 198.61 ± 3.434 μg mL^{-1}, 117.11 ± 3.434 μg mL^{-1}, and 110.21 ± 3.434 μg mL^{-1}, respectively, representing the concentration at which 50% mortality was achieved, as illustrated in Fig. 4D(d).

3.4.3.3 Proteinase inhibitory assay. The proteinase inhibitory assay for biosynthesized EC-AMIONPs is illustrated in Fig. 4E. EC-AMIONPs demonstrated significant anti-proteinase activity across various concentrations, achieving a maximum inhibition of 73.36% at 200 μg mL^{-1}. In comparison, diclofenac sodium reached a maximum inhibition of 74.97% at the same concentration, while the EC extract displayed an inhibition level of 50.66% as shown in Fig. 4E(e). The IC_{50} values were calculated as follows: EC extract, 198.61 ± 1.490 μg mL^{-1}; control, 110.93 ± 1.490 μg mL^{-1}; and EC-AMIONPs, 110.08 ± 1.490 μg mL^{-1}. The concentration required to achieve 50% mortality is depicted in Fig. 4E(f).

3.4.4 Anti-oxidant activity. The DPPH free radical scavenging assay for biosynthesized EC-AMIONPs is presented in Fig. 4F. EC-AMIONPs exhibited the highest antioxidant activity at a concentration of 100 μg mL^{-1}, recording an activity of 80.75%. This was higher than the plant extract's activity of 56.34% and the control's activity of 84.24% (see Fig. 4E(g)). The antioxidant activity increased with higher concentrations of EC-AMIONPs. The IC_{50} values for BHT and EC-AMIONPs were determined to be 39.26 ± 1.32 μg mL^{-1} and 37.68 ± 1.32 μg mL^{-1}, respectively, as shown graphically in Fig. 4F(h).

3.5 Cytotoxicity activity

In the cytotoxicity test, *A. salina* was exposed to various concentrations of EC-AMIONs, yielding impressive results compared to normal saline water (Fig. 5). The mortality rate ranged from 24.33% to 65.00% at concentrations of EC-AMIONPs between 40 and 400 μg mL^{-1}. The highest lethality was observed with the EC extract, surpassing both the EC-AMIONPs and the control. Notably, at a concentration of 400 μg mL^{-1}, the mortality rate peaked at 65.00% (Fig. 5a). The IC_{50} values, indicating the concentration required to achieve 50% mortality, were determined to be 95.90 ± 6.574 μg mL^{-1} for the control, 155.56 ± 6.574 μg mL^{-1} for the EC extract, and 101.52 ± 6.574 μg mL^{-1} for EC-AMIONPs, as illustrated in Fig. 5b. Overall, the study indicates that EC-AMIONPs exhibit lower cytotoxicity against *A. salina*.

3.6 Anticancer activity

3.6.1 Determination of EAC cell viability. The effect of EC-AMIONPs on EAC cell-induced cancer in mice was evaluated by counting cells in a hemocytometer using trypan blue dye. Fig. 6a demonstrates the anticancer activity of EC-AMIONPs across different mouse groups in relation to cell viability. The group treated with EC-AMIONPs exhibited significantly reduced EAC cell viability at 95.82 ± 2.405%, comparable to the standard drug doxorubicin group, which had a viability of 74.27 ± 2.405%. In contrast, the affected group showed an EAC cell viability of 132.67 ± 2.405%, similar to the EC extract-treated group at 122.33 ± 2.405%.

3.6.2 Measurement of EAC cell growth inhibition. The biosynthesized EC-AMIONPs demonstrated a significant inhibition of EAC cell growth, as illustrated in Fig. 6b. The growth inhibition rate for EC-AMIONPs was 89.70 ± 0.167%, compared to 88.60 ± 0.167% for doxorubicin. In contrast, the EC extract exhibited a lower inhibition rate of 43.87 ± 0.167%.

3.6.3 Measurement of body weight and blood glucose level. Fig. 6c illustrates changes in body weight over a 15-day period. Group 1 (normal control) experienced a slight increase in weight from 33.25 ± 2.71 g to 34.75 ± 2.71 g. Groups 2–6 received EAC cell injections on day 0, leading to weight gain by day 3, which confirmed cancer induction. Following treatment

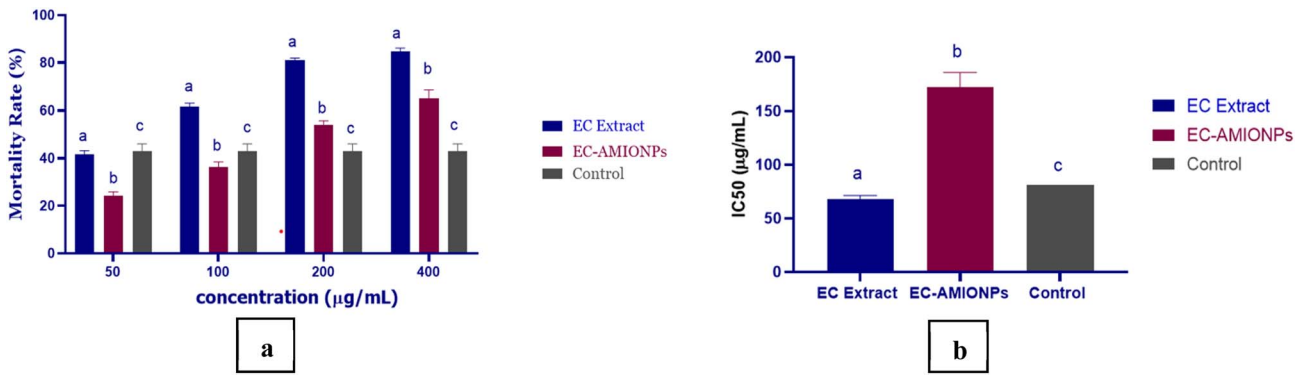

Fig. 5 Mortality percentage (a) and the IC_{50} value (b) of EC-AMIONPs, saline water used as control, and EC extract.

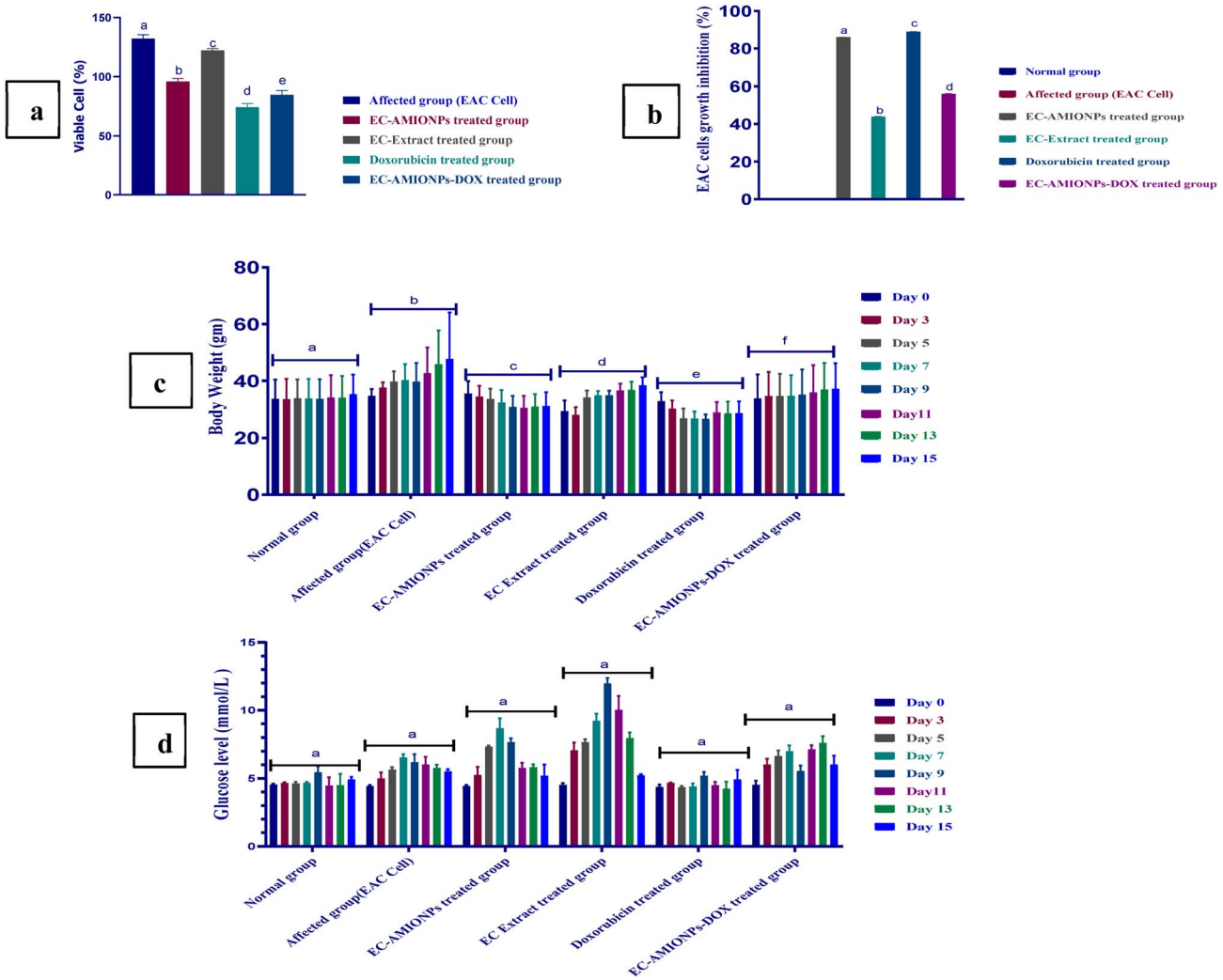

Fig. 6 The percentage of EAC cell viability (a), the percentage of EAC cell growth inhibition (b), the changes of body weight (c) and blood glucose levels (d) of different EAC cell-induced mice groups after treatment with EC-AMIONPs compared to the standard drug and affected group.

initiation in groups 3–6, the untreated EAC group (group 2) continued to gain weight, reaching 53.45 ± 2.71 g by day 15. Group 3 (treated with EC-AMIONPs) initially gained weight until day 5 but then declined to 30.50 ± 2.71 g by day 15, similar to the doxorubicin group. Fig. 6d presents blood glucose levels. All groups maintained normal glucose levels on day 0. Group 1 remained stable, with levels ranging from 4.5 ± 0.92 to 4.9 ± 0.92 mmol L^{-1}. Group 2 also showed stable glucose levels, fluctuating between 4.5 ± 0.92 and 4.9 ± 0.92 mmol L^{-1}. Group 3's glucose peaked at 8.4 ± 0.92 mmol L^{-1} on day 7 but returned to normal levels (4.7 ± 0.92 mmol L^{-1}) by day 15. The doxorubicin group consistently maintained normal glucose levels (4.6 ± 0.92 mmol L^{-1}) throughout the study.

3.6.4 Determination of biochemical, hematological, and ionic parameters. Mice treated with EC-AMIONPs exhibited nearly normal ALT levels (165 U L^{-1}), comparable to both normal mice (150 U L^{-1}) and those treated with doxorubicin (154 U L^{-1}). In contrast, EAC mice displayed elevated ALT levels (250 U L^{-1}), indicating liver damage (Fig. 7a). Creatinine levels in EC-AMIONPs-treated mice were closer to normal (0.7 mg dL^{-1}) compared to the elevated levels found in EAC mice (1.9 mg dL^{-1}) (Fig. 7b). Triglyceride levels increased from 75 mg dL^{-1} in normal mice to 198 mg dL^{-1} in EAC mice but decreased to 85 mg dL^{-1} following EC-AMIONPs treatment (Fig. 7c). Total cholesterol rose from 140 mg dL^{-1} to 195.5 mg dL^{-1} in EAC mice, while EC-AMIONPs treatment reduced it to 173 mg dL^{-1}, a level similar to that seen in doxorubicin-treated mice (180.3 mg dL^{-1}) (Fig. 7d).

Sodium levels were significantly lower in the affected group (131 mmol L^{-1}) compared to normal levels (145.2 mmol L^{-1}), likely due to tumor-related imbalances. However, EC-AMIONPs treatment improved sodium levels to 141 mmol L^{-1} (Fig. 7e). Chloride levels decreased in EAC mice (110.4 mmol L^{-1}) and doxorubicin-treated mice (111.3 mmol L^{-1}), but EC-AMIONPs partially restored chloride levels to 112.7 mmol L^{-1} (Fig. 7f). Potassium levels were elevated in EAC mice (3.9 mmol L^{-1}) and even higher in EC-AMIONPs-treated mice (4.9 mmol L^{-1}), whereas doxorubicin-treated mice maintained levels close to

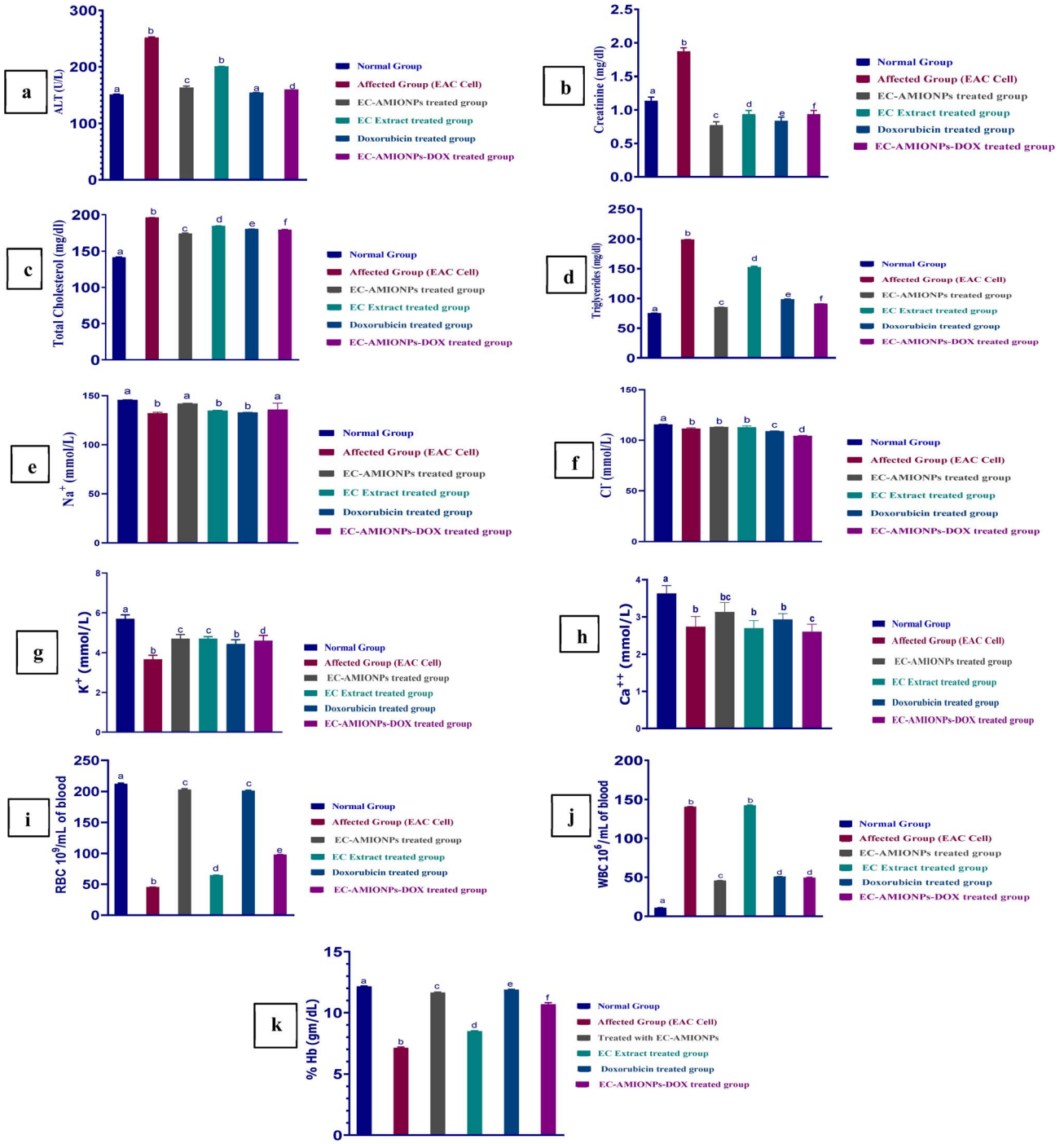

Fig. 7 The alanine aminotransferase (ALT) level (a), total creatinine level (b), triglycerides level (c), total cholesterol level (d), sodium level (e), chloride level (f), total potassium level (g), calcium level (h), red blood cell (RBC) count (i), white blood cell (WBC) count (j), percentage of Hb level (k), after treatment with EC-AMIONPs compared to the standard drug and affected group.

normal (~4.2 mmol L^{-1}) (Fig. 7g). Serum calcium levels dropped in EAC mice (2.44 mmol L^{-1}) but were restored to 3.1 mmol L^{-1} with EC-AMIONPs treatment, indicating protective effects (Fig. 7h).

In the EAC control group, the RBC count significantly decreased to 45.5 × 10^9 mL^{-1} from 211 × 10^9 mL^{-1} in the normal group, suggesting tumor-induced anemia (Fig. 7i). Treatment with EC-AMIONPs improved the RBC count to 204 × 10^9 mL^{-1}, which is comparable to the count in the doxorubicin group (201 × 10^9 mL^{-1}). The EAC group also exhibited marked leukocytosis, with WBC counts rising to 141 × 10^6 mL^{-1} compared to 10 × 10^6 mL^{-1} in normal mice (Fig. 7j). EC-AMIONPs treatment moderately restored WBC levels to 45 × 10^6 mL^{-1}, similar to the doxorubicin group (50 × 10^6 mL^{-1}). Hemoglobin levels fell to 7.1 g dL^{-1} in the affected group but were significantly increased to 11.7 g dL^{-1} with EC-AMIONPs

treatment, approaching the normal level of 12.2 g dL^{-1} (Fig. 7k). This highlights the potential of EC-AMIONPs to alleviate anemia and support hematopoiesis.

3.6.5 Histological analysis. The kidney sections from EAC cell-induced mice exhibited glomerular atrophy, tubular degeneration, and inflammatory infiltration, indicating renal impairment due to tumor burden (Fig. 8a.B). A similar pattern was observed in the EC-extract treated mice (Fig. 8a.D) compared to the normal group (Fig. 8a.A). In contrast, the EC-AMIONPs-treated group (Fig. 8a.C) showed well-preserved glomerular and tubular structures, with significantly reduced necrosis and inflammation. Comparable results were noted in both the DOX-treated group (Fig. 8a.E) and the EC-AMIONPs-DOX-treated group (Fig. 8a.F), suggesting a reno-protective effect of EC-AMIONPs. In the intestinal analysis, EAC cell-induced mice displayed significant villous atrophy, crypt degeneration, and epithelial erosion, indicating tumor-induced intestinal damage (Fig. 8b.B). Conversely, both the EC-AMIONPs-treated group (Fig. 8b.C) and the EC-AMIONPs-DOX-treated group (Fig. 8b.F) showed well-preserved intestinal mucosa, improved villous integrity, reduced crypt damage, and restored epithelial lining, demonstrating strong protective and reparative potential. The DOX-treated group (Fig. 8b.E) also exhibited a mucosal structure similar to that of the normal group (Fig. 8b.A), while the EC-extract treated group (Fig. 8b.D) showed no mucosal recovery, with only mild epithelial reformation. Histological examination of the liver tissue in EAC cell-induced mice revealed severe hepatocellular degeneration, central vein congestion, inflammatory cell infiltration, and focal necrosis, indicating hepatic damage due to tumor progression (Fig. 8c.B). The EC-extract treated group (Fig. 8c.D) showed mild improvement, with partial reductions in necrosis and inflammation. In contrast, the DOX-treated group (Fig. 8c.E) exhibited hepatocellular vacuolation, sinusoidal dilation, and hepatocyte necrosis, consistent with DOX-induced hepatotoxicity. The EC-AMIONPs-DOX-treated group (Fig. 8c.F) displayed a similar liver tissue structure due to the presence of doxorubicin. Notably, the EC-AMIONPs-treated group (Fig. 8c.C) demonstrated improved

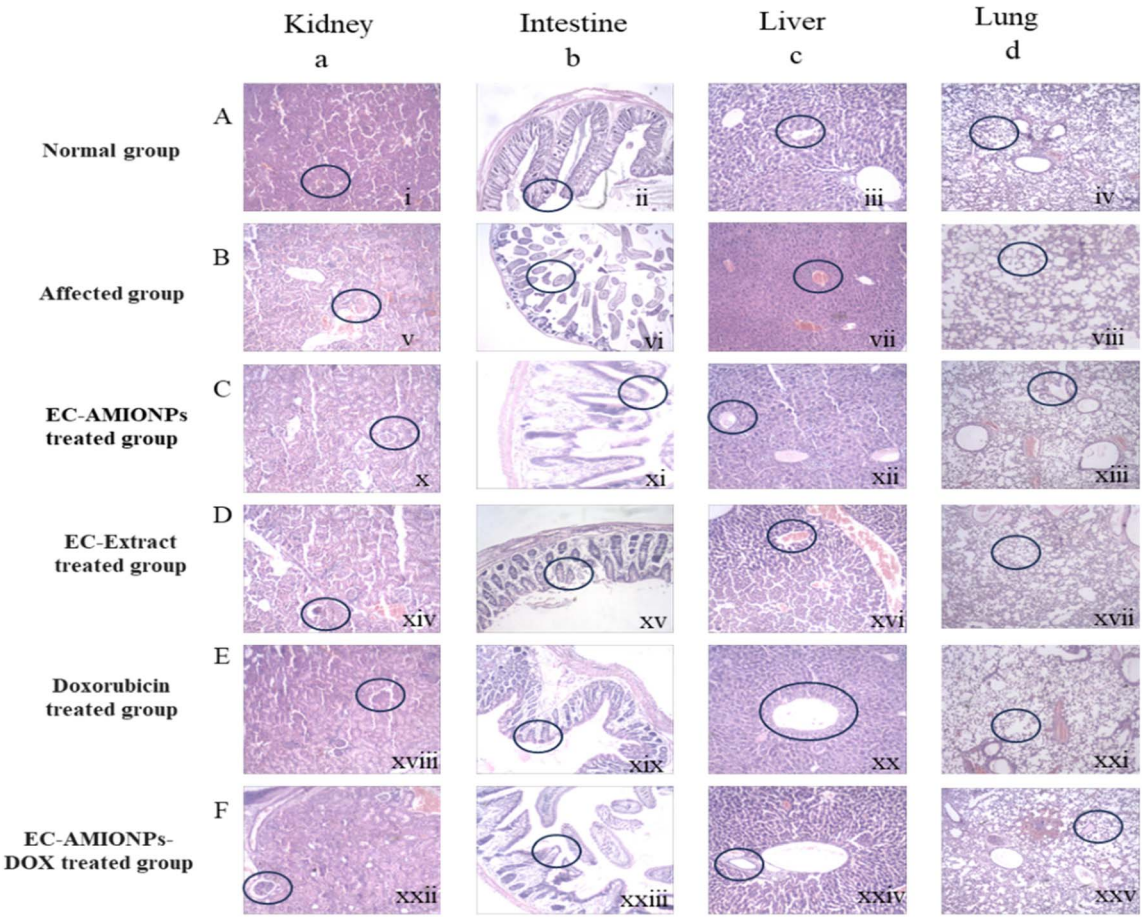

Fig. 8 Histological analysis of Swiss albino mice: (A) normal group; (B) affected group; (C) EC-AMOINPs treated group; (D) EC-extract treated group; (E) doxorubicin treated group; (F) EC-AMOINPs-DOX treated group. Treated kidney tissue (a) showed partial restoration of normal architecture with reduced tubular degeneration and inflammation (i, v, x, xiv, xvii and xxii). Treated intestinal tissue (b) showed partial mucosal regeneration with reduced epithelial damage and inflammation (ii, vi, xi, xv, xix and xxiii). Treated liver tissue (c) exhibited reduced hepatocyte degeneration, decreased inflammatory infiltration, and partial restoration of normal architecture (iii, vii, xii, xvi, xx and xxiv). Treated lung tissue (d) showed reduced tumour infiltration, decreased inflammatory cell infiltration, and partial restoration of alveolar architecture (iv, viii, xiii, xvii, xxi and xxv).

liver architecture with minimal necrotic changes, reduced inflammatory infiltration, and preserved hepatocyte morphology compared to the normal group (Fig. 8c.A), which showed polygonal hepatocytes arranged in uniform cords around the central vein with no visible lesions, suggesting effective hepatoprotection. Histological examination of lung tissues in the normal group displayed clearly defined alveolar spaces (Fig. 8d.A). In contrast, the affected group showed alveolar thickening, congestion, and inflammatory cell infiltration, indicating tumor-associated pulmonary damage (Fig. 8d.B). However, the EC-AMIONPs group (Fig. 8d.C) exhibited largely intact lung architecture, with reduced congestion and minimal inflammatory cell infiltration. Similar results were observed in the doxorubicin-treated group (Fig. 8d.E) and the EC-AMIONPs-DOX-treated group (Fig. 8d.F), which demonstrated the most significant improvement in lung morphology. The EC-extract treated group (Fig. 8d.D) displayed moderate recovery with a partial reduction in inflammatory infiltration.

4. Discussion

Nanobiotechnology holds considerable promise for the field of medicine, particularly through the utilization of superparamagnetic iron oxide nanoparticles (SPIONs). The precise synthesis of these nanoparticles, achieved through controlled co-precipitation of Fe(II) and Fe(III) at elevated temperatures, optimizes their size, dispersibility, and surface characteristics, thereby enhancing their *in vivo* performance, including biodistribution and pharmacokinetics. While conventional physical and chemical synthesis methods can be expensive and environmentally detrimental, biological approaches that employ plant materials offer a simpler, faster, eco-friendly, and non-toxic alternative. These methods result in stable nanoparticles with a high surface area, rendering them suitable for medical applications.[58,59] Consequently, this research utilized both chemical and biological methods to synthesize iron oxide nanoparticles using *E. cardamomum* and evaluated their biological applications.

Following the synthesis of the nanoparticles, confirmation and characterization are critical steps. A color change from light red to dark red signifies the formation of iron oxide nanoparticles. This observation is further validated by UV-visible spectroscopy, which displays a strong absorption peak within the range of 219 to 275 nm, aligning with the typical UV absorption spectrum of 200–300 nm for green-synthesized iron oxide nanoparticles.[60] FTIR analysis substantiates the formation of iron oxide nanoparticles, as evidenced by a prominent Fe–O peak at 570–580 cm^{-1}, which is slightly reduced due to organic coating. Additionally, a Si–O peak at 1138 cm^{-1} indicates a core–shell structure and successful salinization. The presence of ATPMS propyl groups is confirmed by the C–H peak at 2924 cm^{-1}. Shifts observed at 3408 cm^{-1} (N–H, O–H) suggest hydrogen bonding, while a peak at 1650 cm^{-1} (CONH) signifies amide linkage with *E. cardamomum* biomolecules, corroborating findings from previous studies.[61,62] The size of the synthesized EC-AMIONPs was confirmed to be 10.23 nm through SEM analysis, with a prior study reporting similarly sized green-synthesized iron oxide nanoparticles at 12.61 nm.[62] XRD analysis determined the size of AMIONPs to be 14.48 nm using the Debye–Scherrer equation, which closely aligns with the SEM results. In contrast, Karpagavinayagam *et al.* (2018) reported Fe NPs measuring 45.09 nm utilizing marine flower extract.[63] The XRD peaks of EC-AMIONPs exhibited an amorphous state, akin to previously synthesized particles, lacking distinct peaks that would indicate impurities. EDX analysis confirmed the purity of the synthesized EC-AMIONPs, revealing an iron content of 43.40%. Thermal stability, assessed through TGA, indicated a 40% weight loss at 800 °C, primarily attributed to the evaporation of absorbed water. The stable weight observed thereafter reflects good thermal stability, rendering them suitable for applications in animal models.[64] The magnetic properties of EC-AMIONPs, analyzed using a vibrating sample magnetometer, confirmed their paramagnetic nature, making them ideal for biomedical applications.[65]

Preliminary phytochemical analysis of EC-AMIONPs indicated the presence of alkaloids, steroids, tannins, and terpenoids. Cardamom oil, extracted through steam distillation and Soxhlet extraction, demonstrated positive results for carbohydrates, proteins, steroids, glycosides, alkaloids, and terpenoids. These secondary metabolites are recognized for their diverse biological and therapeutic benefits.[66–69]

EC-AMIONPs exhibited strong antibacterial and antibiofilm activity against multidrug-resistant Gram-positive and Gram-negative bacteria, exceeding the effectiveness of the control drug, clarithromycin. The APTMS $-NH_2$ groups facilitate efficient cardamom loading, enhancing nanoparticle stability and bioavailability, while functionalized nanoparticles improve antibacterial activity *via* reactive oxygen species (ROS) and phytochemicals.[70–73] In contrast, the *E. cardamomum* extract alone exhibited weaker activity, consistent with previous reports attributing its efficacy to phenolic and terpenoid compounds capable of disrupting bacterial membranes and metabolic enzymes; however its effectiveness may vary with concentration, solvent, and phytochemical content.[74] Previous studies indicated that uncoated IONPs exhibited stronger antibacterial activity than cardamom extract due to ROS generation and Fe^{2+}/Fe^{3+}-induced oxidative stress, leading to bacterial membrane damage.[72,75] Therefore, the enhanced antibacterial effect of EC-AMIONPs is attributed to bioactive compounds (phenolic compounds, flavonoids, and terpenoids) in the extract, which stabilize and cap the AMIONPs, thereby increasing their therapeutic potential.[34] The DPPH assay assessed the antioxidant activity of EC-AMIONPs, revealing a strong inhibition rate of 80.75 ± 0.44% with an IC_{50} of 37.68 μg mL^{-1}, significantly higher than 56.34% observed for the EC extract. This increased activity is likely due to the bioactive compounds from *E. cardamomum* that have been functionalized with AMIONPs, allowing for stable phytochemical release. Previous studies also support the strong antioxidant potential of plant-based iron oxide nanoparticles.[76]

The anti-inflammatory activity of EC-AMIONPs was evaluated through albumin denaturation, proteinase inhibition, and human red blood cell (HRBC) membrane stabilization assays, yielding effectiveness rates of 76.92%, 73.36%, and 78.85%,

respectively, at a concentration of 200 μg mL^{-1}. These findings demonstrate a strong anti-inflammatory potential that often matches or exceeds that of diclofenac sodium. Compared to the plant extract alone, EC-AMIONPs exhibited superior effects. Their nanoparticle-based structure, combined with bioactive compounds from *E. cardamomum*, enhances bioavailability, facilitates targeted delivery, and promotes sustained release, positioning them as a promising and safer alternative for anti-inflammatory therapy.[77–79]

The cytotoxicity of EC-AMIONPs was assessed using the *Artemia salina* lethality assay, revealing a dose-dependent increase in mortality from 24.33% to 65.00% at concentrations ranging from 40 to 400 μg mL^{-1}. The LC_{50} was determined to be 101.52 ± 6.57 μg mL^{-1}, indicating relatively low toxicity compared to the control. This suggests that EC-AMIONPs are safer than the *E. cardamomum* extract alone, supporting their potential as a bioactive yet less toxic alternative, consistent with previous findings.[80,81] Overall characterization confirmed that the synthesized particles were indeed EC-AMIONPs, which exhibit multiple applications, including antioxidant, antibacterial, antibiofilm, anti-inflammatory activities, and cytotoxicity.

The biosynthesized EC-AMIONPs demonstrated significant anticancer effects by inhibiting EAC cell growth in mice. At a dosage of 0.2 mg kg^{-1} day^{-1}, they reduced cell viability by 95.82 ± 0.98%, outperforming control treatments. At 0.1 mg kg^{-1}, they achieved an 85.8 ± 0.37% inhibition, comparable to doxorubicin's 88.73 ± 0.37%. Additionally, EC-AMIONPs reduced cholesterol and triglyceride levels, restored near-normal ALT and creatinine levels, and improved electrolyte balance by normalizing sodium, calcium, potassium, and chloride levels. Hematological assessments revealed increased RBC count and restored WBC and hemoglobin levels, indicating a reversal of tumor-induced anemia and providing immune support. Histologically, EC-AMIONPs preserved the architecture of liver, kidney, lung, and intestinal tissues, demonstrating protective effects against tumor-induced damage and suggesting significant renal and pulmonary protective benefits. The nanoparticles generate ROS and, in conjunction with cardamom phytochemicals (flavonoids, terpenoids, phenolic acids), induce oxidative stress and mitochondrial dysfunction. The APTMS coating enhances stability and sustained release, collectively triggering apoptosis, autophagy, and cell cycle arrest to inhibit cancer cell proliferation.[82–84] Parameters such as serum biochemical analysis, ionic analysis, hematological analysis, and histopathological analysis were conducted to confirm the anticancer activity of EC-AMIONPs. The results of EC-AMIONPs indicate that EC-AMIONPs may serve as a potential therapeutic agent with substantial effects on metabolic disturbances, organ protection, and hematological restoration in cancer-induced mice. The functional coatings on nanoparticles not only enhance their ROS-mediated cytotoxicity, colloidal stability, and biocompatibility but also allow for controlled interactions with biological targets, improving specificity and efficacy, with potential for future theragnostic applications.[73,85–87]

5. Conclusion

The present study demonstrates the synthesis of iron oxide nanoparticles through a co-precipitation method integrated with a biological approach, which is characterized as simple, cost-effective, and environmentally friendly. The extract of *E. cardamomum* functioned as both a stabilizing and reducing agent, while APTMS was employed to modify the surface of the iron nanoparticles. Characterization techniques—including UV-vis, FTIR, SEM, XRD, TGA, and VSM—confirmed the nanoparticles' spherical morphology, functional groups, thermal stability, and magnetic properties. The analysis revealed the presence of phytochemicals such as steroids, terpenoids, alkaloids, tannins, and phenols. The EC-AMIONPs exhibited enhanced biological activities, including cytotoxicity, antibacterial, antioxidant, anti-inflammatory, and antitumor effects, in comparison to the seed extract. The brine shrimp assay substantiated the cytotoxicity, while antibacterial assessments demonstrated efficacy against various pathogens. *In vivo* studies indicated anticancer potential and improvements in biochemical and histological parameters in mice. These findings suggest that EC-AMIONPs hold significant promise for therapeutic applications; however, further research is necessary.

Author contributions

Conceptualization, S. B. R. G., and M. A. S.; methodology, S. B. R. G., S. P., M. A. M., M. F. H.; validation, M. A.-E-E., M. S. U., T. H.; formal analysis, S. B. R. G., S. P., M. A. M., M. F. H.; investigation, S. B. R. G., S. P., M. A. M., M. F. H.; resources, M. F. H., T. H., S. Z., M. A. S.; writing – original draft preparation, S. B. R. G., S. P.; writing – review and editing, S. Z.; and M. A. S.; supervision, S. Z., and M. A. S.; all authors have read and agreed to the published version of the manuscript.

Conflicts of interest

The author declares no conflict of interest.

Ethical approval and consent to participate

All experimental protocols completed in our study, including animals, were approved by the Institutional Animal, Medical Ethics, Bio-safety and Bio-security Committee (IAMEBBC) for Experimentations on Animal, Human, Microbes and Living Natural Sources, Institute of Biological Sciences, University of Rajshahi, Bangladesh (memo no.: 203/320(69)/IAMEBBC/IBSc), according to the International Declaration of Helsinki. Informed consents were obtained from human participants of this study.

Data availability

The datasets used and/or analyzed during the current study are available from the corresponding author upon reasonable request.

Acknowledgements

The authors are grateful to the Ministry of Science and Technology, Government of the People's Republic of Bangladesh, for funding this research (Grant No. SRG-251324; 2025–2026).

References

1 S. Sadeghi, et al., Anti-cancer effects of cinnamon: Insights into its apoptosis effects, *Eur. J. Med. Chem.*, 2019, **178**, 131–140.
2 W. Tan, et al., Anti-cancer natural products isolated from Chinese medicinal herbs, *Chin. Med.*, 2011, **6**(1), 27.
3 Q. Ye, et al., Iron and zinc ions, potent weapons against multidrug-resistant bacteria, *Appl. Microbiol. Biotechnol.*, 2020, **104**, 5213–5227.
4 A. Sultana, M. Zare, V. Thomas, T. S. S. Kumar and S. Ramakrishna, Nano-based drug delivery systems: Conventional drug delivery routes, recent developments and future prospects, *Med. Drug Discovery*, 2022, **15**, 100134.
5 H. Nejat, et al., Preparation and characterization of cardamom extract-loaded gelatin nanoparticles as effective targeted drug delivery system to treat glioblastoma, *React. Funct. Polym.*, 2017, **120**, 46–56.
6 V. Omprakash and S. Sharada, Green synthesis and characterization of silver nanoparticles and evaluation of their antibacterial activity using Elettaria cardamom seeds, *J. Nanomed. Nanotechnol.*, 2015, **6**(2), 1–4.
7 I. Hussain, N. B. Singh, A. Singh, H. Singh and S. C. Singh, Green synthesis of nanoparticles and its potential application, *Biotechnol. Lett.*, 2016, **38**, 545–560.
8 L. Guo, et al., Smart hydrogel: A new platform for cancer therapy, *Adv. Colloid Interface Sci.*, 2025, 103470.
9 P. Wu, et al., Aptamer-AuNP-conjugated carboxymethyl chitosan–functionalized graphene oxide for colorimetric identification of Salmonella typhimurium, *Microchim. Acta*, 2022, **189**(11), 408.
10 Y. Wu, Q. Y. Liu, Z. Q. Bu, M. X. Quan, J. Y. Lu and W. T. Huang, Colorimetric multi-channel sensing of metal ions and advanced molecular information protection based on fish scale-derived carbon nanoparticles, *Spectrochim. Acta, Part A*, 2023, **290**, 122291.
11 S. Stanley, Biological nanoparticles and their influence on organisms, *Curr. Opin. Biotechnol.*, 2014, **28**, 69–74.
12 R. Misra, S. Acharya and S. K. Sahoo, Cancer nanotechnology: application of nanotechnology in cancer therapy, *Drug Discovery Today*, 2010, **15**(19–20), 842–850.
13 P. K. D. Pramanik, A. Solanki, A. Debnath, A. Nayyar, S. El-Sappagh and K.-S. Kwak, Advancing modern healthcare with nanotechnology, nanobiosensors, and internet of nano things: Taxonomies, applications, architecture, and challenges, *IEEE Access*, 2020, **8**, 65230–65266.
14 S. Anjum, et al., Emerging applications of nanotechnology in healthcare systems: Grand challenges and perspectives, *Pharmaceuticals*, 2021, **14**(8), 707.
15 M. Thakur, A. Sharma, M. Chandel and D. Pathania, Modern applications and current status of green nanotechnology in environmental industry, in *Green Functionalized Nanomaterials for Environmental Applications*, Elsevier, 2022, pp. 259–281.
16 W. Wu, Q. He and C. Jiang, Magnetic iron oxide nanoparticles: synthesis and surface functionalization strategies, *Nanoscale Res. Lett.*, 2008, **3**, 397–415.
17 S. Prijic and G. Sersa, Magnetic nanoparticles as targeted delivery systems in oncology, *Radiol. Oncol.*, 2011, **45**(1), 1.
18 S. Bano, N. Ahmad and A. K. Sharma, Phytochemical screening and evaluation of anti-microbial and anti-oxidant activity of Elettaria cardamom (Cardamom), *J. Appl. Nat. Sci.*, 2016, **8**(4), 1966–1970.
19 K. Ashokkumar, M. Murugan, M. K. Dhanya and T. D. Warkentin, Botany, traditional uses, phytochemistry and biological activities of cardamom [Elettaria cardamomum (L.) Maton]–A critical review, *J. Ethnopharmacol.*, 2020, **246**, 112244.
20 A. Heydarian, N. Tahvilian, H. Shahinfar, S. A. Abbas-Hashemi, R. Daryabeygi-Khotbehsara and N. Aryaeian, Effect of cardamom consumption on inflammation and blood pressure in adults: A systematic review and meta-analysis of randomized clinical trials, *Food Sci. Nutr.*, 2024, **12**(1), 3–12.
21 S. Qiblawi, M. A. Kausar, S. M. A. Shahid, M. Saeed and A. Y. Alazzeh, Therapeutic interventions of cardamom in cancer and other human diseases, *J. Pharm. Res. Int.*, 2020, **32**(22), 74–84.
22 H. Kaur, S. Kumar, G. Kaur, N. Kaur, R. Badru and R. Saini, An emerging expanse: Novel and eco-friendly-biogenic synthesis of E. cardamomum-wrapped TiO_2 nanoparticles for environmental and biological applications, *Environ. Res.*, 2023, **234**, 116599.
23 A. Kiran, et al., Green synthesis of NiO and NiO@graphene oxide nanomaterials using Elettaria cardamomum leaves: Structural and electrochemical studies, *Heliyon*, 2024, **10**(20), e38613.
24 S. Zubair Dhabian and R. Sabeeh Jasim, Antioxidant, Cytotoxic, and Antihemolytic Activity of Greenly Synthesized Selenium Nanoparticles Using Elettaria Cardamomum Extract, *J. Nanostruct.*, 2023, **13**(1), 76–85.
25 S. Pal, K. Pal, S. Mukherjee, D. Bera, P. Karmakar and D. Sukhen, Green cardamom mediated phytosynthesis of ZnONPs and validation of its antibacterial and anticancerous potential, *Mater. Res. Express*, 2020, **7**(1), 15068.
26 A. Venkatramanan, A. Ilangovan, P. Thangarajan, A. Saravanan and B. Mani, Green synthesis of copper oxide nanoparticles (CuO NPs) from aqueous extract of seeds of Elettaria cardamomum and its antimicrobial activity against pathogens, *Curr. Biotechnol.*, 2020, **9**(4), 304–311.
27 V. Soshnikova, et al., Cardamom fruits as a green resource for facile synthesis of gold and silver nanoparticles and their biological applications, *Artif. Cells, Nanomed., Biotechnol.*, 2018, **46**(1), 108–117.
28 D. GingaŞu, et al., Green synthesis of cobalt ferrite nanoparticles using plant extracts, *Rev. Roum. Chim.*, 2017, **62**(8–9), 645–653.

29 P. Khatri, J. S. Rana, P. Jamdagni and A. Sindhu, Phytochemical screening, GC-MS and FT-IR analysis of methanolic extract leaves of Elettaria cardamomum, *Int. J. Res.*, 2017, **5**(2), 213–224.
30 S. Laurent, et al., Magnetic iron oxide nanoparticles: synthesis, stabilization, vectorization, physicochemical characterizations, and biological applications, *Chem. Rev.*, 2008, **108**(6), 2064–2110.
31 M. J. Palimi, M. Rostami, M. Mahdavian and B. Ramezanzadeh, Surface modification of Fe_2O_3 nanoparticles with 3-aminopropyltrimethoxysilane (APTMS): An attempt to investigate surface treatment on surface chemistry and mechanical properties of polyurethane/Fe_2O_3 nanocomposites, *Appl. Surf. Sci.*, 2014, **320**, 60–72.
32 S. Vikram, R. Vasanthakumari, T. Tsuzuki and M. Rangarajan, Investigations of suspension stability of iron oxide nanoparticles using time-resolved UV–visible spectroscopy, *J. Nanopart. Res.*, 2016, **18**, 1–24.
33 D. Bharathi, M. Diviya Josebin, S. Vasantharaj and V. Bhuvaneshwari, Biosynthesis of silver nanoparticles using stem bark extracts of Diospyros montana and their antioxidant and antibacterial activities, *J. Nanostruct. Chem.*, 2018, **8**, 83–92.
34 S. Perveen, et al., Green synthesis of iron (Fe) nanoparticles using Plumeria obtusa extract as a reducing and stabilizing agent: Antimicrobial, antioxidant and biocompatibility studies, *Arabian J. Chem.*, 2022, **15**(5), 103764.
35 M. V Arularasu, J. Devakumar and T. V Rajendran, An innovative approach for green synthesis of iron oxide nanoparticles: Characterization and its photocatalytic activity, *Polyhedron*, 2018, **156**, 279–290.
36 A. K. Gupta and M. Gupta, Synthesis and surface engineering of iron oxide nanoparticles for biomedical applications, *Biomaterials*, 2005, **26**(18), 3995–4021.
37 J. Parekh and S. Chanda, In vitro antimicrobial activity and phytochemical analysis of some Indian medicinal plants, *Turk. J. Biol.*, 2007, **31**(1), 53–58.
38 J. Senguttuvan, S. Paulsamy and K. Karthika, Phytochemical analysis and evaluation of leaf and root parts of the medicinal herb, Hypochaeris radicata L. for in vitro antioxidant activities, *Asian Pac. J. Trop. Biomed.*, 2014, **4**, S359–S367.
39 S. Shresta, et al., Evaluation of phytochemical, antioxidant and antibacterial activities of selected medicinal plants, *Nepal J. Biotechnol.*, 2021, **9**(1), 50–62.
40 A. Nisar, A. S. Mamat, M. I. Hatim, M. S. Aslam and M. Syarhabil, An updated review on Catharanthus roseus: phytochemical and pharmacological analysis, *Indian Res. J. Pharm. Sci.*, 2016, **3**(2), 631–653.
41 M. S. Uddin, et al., Phytochemical analysis and antioxidant profile of methanolic extract of seed, pulp and peel of Baccaurea ramiflora Lour., *Asian Pac. J. Trop. Med.*, 2018, **11**(7), 443–450.
42 J. Jeyasundari, P. S. Praba, Y. B. A. Jacob, V. S. Vasantha and V. Shanmugaiah, Green synthesis and characterization of zero valent iron nanoparticles from the leaf extract of Psidium guajava plant and their antibacterial activity, *Chem. Sci. Rev. Lett.*, 2017, **6**(22), 1244–1252.
43 G. A. O'Toole, Microtiter dish biofilm formation assay, *J. Visualized Exp.*, 2011, (47), e2437.
44 F. Erci and R. Cakir-Koc, Rapid green synthesis of noncytotoxic iron oxide nanoparticles using aqueous leaf extract of Thymbra spicata and evaluation of their antibacterial, antibiofilm, and antioxidant activity, *Inorg. Nano-Met. Chem.*, 2020, **51**(5), 683–692.
45 S. E. Priani, S. Aprilia, R. Aryani and L. Purwanti, Antioxidant and tyrosinase inhibitory activity of face serum containing cocoa pod husk phytosome (Theobroma cacao L.), *J. Appl. Pharm. Sci.*, 2019, **9**(10), 110–115.
46 A. Alam and V. Singh, Composition and pharmacological activity of essential oils from two imported Amomum subulatum fruit samples, *J. Taibah Univ. Med. Sci.*, 2021, **16**(2), 231–239.
47 A. Selvaraj, A. M. George and R. Shanmugam, Biosynthesis, Characterization, And Anti-Inflammatory Activity Of Silver Nanoparticles Using Novel Clove And Cardamom Plant Extract-Invitro Study, *J. Pharm. Negat. Results*, 2022, 4409–4419.
48 Y. Nagaharika and S. Rasheed, Anti-inflammatory activity of leaves of Jatropha gossypifolia L. by HRBC membrane stabilization method, *J Acute Dis.*, 2013, **2**(2), 156–158.
49 K. D. P. P. Gunathilake, K. K. D. S. Ranaweera and H. P. V. Rupasinghe, In vitro anti-inflammatory properties of selected green leafy vegetables, *Biomedicines*, 2018, **6**(4), 107.
50 V. Balamurugan and G. Balasubramani, Green synthesis and cytotoxicity evaluation of silver and gold nanoparticles using Pandanus canaranus leaf extract on Artemia salina and A549 lung cancer cells, *Biomass Convers. Biorefin.*, 2024, **14**(13), 14433–14446.
51 S. Rajabi, A. Ramazani, M. Hamidi and T. Naji, Artemia salina as a model organism in toxicity assessment of nanoparticles, *Daru, J. Pharm. Sci.*, 2015, **23**, 1–6.
52 A. H. M. K. Alam, et al., The antioxidative fraction of white mulberry induces apoptosis through regulation of p53 and NFκB in EAC cells, *PLoS One*, 2016, **11**(12), e0167536.
53 S. V Kalish, S. V Lyamina, E. A. Usanova, E. B. Manukhina, N. P. Larionov and I. Y. Malyshev, Macrophages reprogrammed in vitro towards the M1 phenotype and activated with LPS extend lifespan of mice with ehrlich ascites carcinoma, *Med. Sci. Monit.: Basic Res.*, 2015, **21**, 226.
54 P. Sur and D. K. Ganguly, Tea plant root extract (TRE) as an antineoplastic agent, *Planta Med.*, 1994, **60**(02), 106–109.
55 A. Pavlovic Markovic, et al., Jaundice as a diagnostic and therapeutic problem: a general practitioner's approach, *Dig. Dis.*, 2022, **40**(3), 362–369.
56 M. V Fargo, S. P. Grogan and A. Saguil, Evaluation of jaundice in adults, *Am. Fam. Physician*, 2017, **95**(3), 164–168.
57 T. B. Lima, et al., In vivo effects of cagaita (Eugenia dysenterica, DC.) leaf extracts on diarrhea treatment, *J. Evidence-Based Complementary Altern. Med.*, 2011, **2011**(1), 309390.

58 K. Li, et al., Magnetic resonance imaging of glioma with novel APTS-coated superparamagnetic iron oxide nanoparticles, *Nanoscale Res. Lett.*, 2014, **9**, 1–11.
59 W. S. Rita, N. K. L. E. Yanti and I. Swantara, Antibacterial Activity and Characterization of Chitosan Nanoparticles Prepared from Hijau Lumut Banana (Musa paradisiaca L.) Peel Ethyl Acetate Extract, *Nano Biomed. Eng.*, 2023, **15**(3), 278–287.
60 M. Pattanayak and P. L. Nayak, Green synthesis and characterization of zero valent iron nanoparticles from the leaf extract of Azadirachta indica (Neem), *World J. Nanosci. Technol.*, 2013, **2**(1), 6–9.
61 K. M. Kumar, B. K. Mandal, K. S. Kumar, P. S. Reddy and B. Sreedhar, Biobased green method to synthesise palladium and iron nanoparticles using Terminalia chebula aqueous extract, *Spectrochim. Acta, Part A*, 2013, **102**, 128–133.
62 J. A. A. Abdullah, L. S. Eddine, B. Abderrhmane, M. Alonso-González, A. Guerrero and A. Romero, Green synthesis and characterization of iron oxide nanoparticles by phoenix dactylifera leaf extract and evaluation of their antioxidant activity, *Sustainable Chem. Pharm.*, 2020, **17**, 100280.
63 P. Karpagavinayagam and C. Vedhi, Green synthesis of iron oxide nanoparticles using Avicennia marina flower extract, *Vacuum*, 2019, **160**, 286–292.
64 S. Lakshminarayanan, M. F. Shereen, K. L. Niraimathi, P. Brindha and A. Arumugam, One-pot green synthesis of iron oxide nanoparticles from Bauhinia tomentosa: Characterization and application towards synthesis of 1,3-diolein, *Sci. Rep.*, 2021, **11**(1), 8643.
65 N. Beheshtkhoo, M. A. J. Kouhbanani, A. Savardashtaki, A. M. Amani and S. Taghizadeh, Green synthesis of iron oxide nanoparticles by aqueous leaf extract of Daphne mezereum as a novel dye removing material, *Appl. Phys. A*, 2018, **124**, 1–7.
66 U. Kumar, B. Kumar, A. Bhandari and Y. Kumar, Phytochemical investigation and comparison of antimicrobial screening of clove and cardamom, *Int. J. Pharm. Sci. Res.*, 2010, **1**(12), 138–147.
67 D. Benedec, et al., Polyphenolic composition, antioxidant and antibacterial activities for two Romanian subspecies of Achillea distans Waldst. et Kit. ex Willd, *Molecules*, 2013, **18**(8), 8725–8739.
68 C. Proestos, K. Lytoudi, O. K. Mavromelanidou, P. Zoumpoulakis and V. J. Sinanoglou, Antioxidant capacity of selected plant extracts and their essential oils, *Antioxidants*, 2013, **2**(1), 11–22.
69 B. G. Rao, E. S. Rao and T. M. Rao, Quantification of phytochemical constituents and in-vitro antioxidant activity of Mesua ferrea leaves, *Asian Pac. J. Trop. Biomed.*, 2012, **2**(2), S539–S542.
70 L. Bong, N. Ng and A. S. A. Keyon, Green Magnetic Adsorbent Functionalized with Humic Acid for Efficient Removal of Saxitoxin from Water, *J. Mater. Life Sci.*, 2025, 38–49.
71 N. Lal, M. Seifan, A. Ebrahiminezhad and A. Berenjian, The impact of amine-functionalised iron oxide nanoparticles on the menaquinone-7 isomer profile and production of the bioactive isomer, *Mol. Biotechnol.*, 2024, **66**(8), 1970–1987.
72 T.-G. Zhang and C.-Y. Miao, Iron oxide nanoparticles as promising antibacterial agents of new generation, *Nanomaterials*, 2024, **14**(15), 1311.
73 L. Zhang, H. Shi, X. Tan, Z. Jiang, P. Wang and J. Qin, Ten-gram-scale mechanochemical synthesis of ternary lanthanum coordination polymers for antibacterial and antitumor activities, *Front. Chem.*, 2022, **10**, 898324.
74 S. Bano, A. Majumder, A. Srivastava and K. B. Nayak, Deciphering the Potentials of Cardamom in Cancer Prevention and Therapy: From Kitchen to Clinic, *Biomolecules*, 2024, **14**, 1166.
75 J. Flieger, et al., Characteristics and antimicrobial activities of iron oxide nanoparticles obtained via mixed-mode chemical/biogenic synthesis using spent hop (Humulus lupulus L.) extracts, *Antibiotics*, 2024, **13**(2), 111.
76 A. U. Mirza, et al., Biogenic synthesis of iron oxide nanoparticles using Agrewia optiva and Prunus persica phyto species: Characterization, antibacterial and antioxidant activity, *J. Photochem. Photobiol., B*, 2018, **185**, 262–274.
77 H. K. Kandikattu, et al., Anti-inflammatory and anti-oxidant effects of Cardamom (Elettaria repens (Sonn.) Baill) and its phytochemical analysis by 4D GCXGC TOF-MS, *Biomed. Pharmacother.*, 2017, **91**, 191–201.
78 S. Arpitha, K. Srinivasan and H. B. Sowbhagya, Anti-inflammatory effect of resin fraction of cardamom (Elettaria cardamomum) in carrageenan-induced rat paw edema, *PharmaNutrition*, 2019, **10**, 100165.
79 M. Souissi, J. Azelmat, K. Chaieb and D. Grenier, Antibacterial and anti-inflammatory activities of cardamom (Elettaria cardamomum) extracts: Potential therapeutic benefits for periodontal infections, *Anaerobe*, 2020, **61**, 102089.
80 Z. Ullah, et al., Eco-friendly Synthesis of Iron Oxide Nanoparticles Using Parietaria alsinifolia Extracts and Evaluation of Biological Applications, *Appl. Biochem. Biotechnol.*, 2025, 1–28.
81 M. Haris, et al., Oscillatoria limnetica mediated green synthesis of iron oxide (Fe_2O_3) nanoparticles and their diverse in vitro bioactivities, *Molecules*, 2023, **28**(5), 2091.
82 A. G. Ranjbary, G. K. Saleh, M. Azimi, F. Karimian, J. Mehrzad and J. Zohdi, Superparamagnetic iron oxide nanoparticles induce apoptosis in HT-29 cells by stimulating oxidative stress and damaging DNA, *Biol. Trace Elem. Res.*, 2023, **201**(3), 1163–1173.
83 Y. Li, et al., Cardamonin induces ROS-mediated G2/M phase arrest and apoptosis through inhibition of NF-κB pathway in nasopharyngeal carcinoma, *Cell Death Dis.*, 2017, **8**(8), e3024.
84 L. E. Woodard, et al., Nanoparticle architecture preserves magnetic properties during coating to enable robust multi-modal functionality, *Sci. Rep.*, 2018, **8**(1), 12706.
85 I. Z. Ahmad, M. Kuddus, H. Tabassum, A. Ahmad and A. Mabood, Advancements in applications of surface

modified nanomaterials for cancer theranostics, *Curr. Drug Metab.*, 2017, **18**(11), 983–999.

86 A. Al-Abboodi, S. Albukhaty, G. M. Sulaiman, M. A. A. J. Al-Saady, M. S. Jabir and M. M. Abomughaid, Protein conjugated superparamagnetic iron oxide nanoparticles for efficient vaccine delivery systems, *Plasmonics*, 2024, **19**(1), 379–388.

87 L. Li, Y. Si, B. He and J. Li, Au-Ag alloy/porous-SiO_2 core/shell nanoparticle-based surface-enhanced Raman scattering nanoprobe for ratiometric imaging analysis of nitric oxide in living cells, *Talanta*, 2019, **205**, 120116.